Effects of ZnO addition on the microstructure/corrosion, wear and mechanical properties of sintered Mg-Al matrix composites

S. Jayasathyakawin [a], M. Ravichandran [a,b,*,] Sikiru Oluwarotimi Ismail [c,*,] G. Veerappan [d]

[a] Department of Mechanical Engineering, K. Ramakrishnan College of Engineering, Samayapuram, Trichy 621112, Tamil Nadu, India

[b] Visiting Professor, Department of Mechanical Engineering & University Centre for Research & Development, Chandigarh University, Mohali-140413, Punjab, India

[c] Department of Engineering, Centre for Engineering Research, School of Physics, Engineering and Computer Science, University of Hertfordshire, Hatfield AL10 9AB, UK

[d] Department of Mechatronics Engineering, Sri Krishna College of Engineering and Technology, Coimbatore 641008, Tamil Nadu, India

*Corresponding authors: M. Ravichandran, smravichandran@hotmail.com, +91 824 8165 224

S. O. Ismail, s.ismail3@herts.ac.uk, +44 17 0728 5213

Abstract

Magnesium (Mg)-based composites offer outstanding properties, which make them suitable materials for various applications in medical, aerospace and energy sectors, among others. The wide applications of Mg-based composites have attracted continuous effort to increase their properties and performances. Therefore, the present work focused on synthesizing magnesium-aluminium-zinc oxide (Mg-Al-ZnO) composites. Mg-3Al-xZnO (x = 3, 6 and 9 wt.%) composites were prepared using powder metallurgy (PM) route. The composite powders and sintered composites were analyzed to determine their microstructures, using scanning electron microscopy (SEM) and energy dispersive X-ray (EDX) analysis. In addition, the sintering process took place in argon atmosphere at 450 ^{o}C. The quantitative analyses of density, porosity, hardness, compressive strength (CS) and corrosion rate (CR) of the composites were performed. Wear performance was also studied with various wear control parameters, such as the sliding velocity (V), sliding distance (D), applied load (P) as well as ZnO content. Pin-on-disc apparatus was used to determine the wear rate (WR) and coefficient of friction (COF) of the innovatively prepared Mg-3wt.%Al-ZnO composites. The experimental study was conducted in accordance with Taguchi's L_{16} orthogonal design.

Signal-to-noise (S/N) ratio analysis was employed to determine the best combination of parameters for WR and COF. Summarily, SEM images confirmed that ZnO particles were uniformly distributed in the composite samples. Statistical technique, called analysis of variance (ANOVA), was adopted to find the significant factor which affected WR and COF. The P significantly affected the WR, followed by the inclusion of ZnO. But, with respect to COF, ZnO reinforcement inclusion affected COF significantly when compared with the P. Both V and D did not affect WR and COF. Hence, the application of the various composite samples should depend on their various responses to friction and wear, especially in working conditions where both quantities are inevitable.

Keywords: Magnesium; Composite; Powder metallurgy; Mechanical properties; Corrosion; Wear, Friction.

1. Introduction

Composite materials have better properties that depend on several factors, such as the matrix, reinforcement materials, interfaces between materials, volume fraction and temperature [1]. Metal matrix composites (MMCs) are commonly used in the wear resistant materials. Also, they have major applications in automotive components, such as piston rings, brake discs, brake rotors and cylindrical linings.

MMCs possess superior properties, including strength, stiffness and creep resistance. The automotive industry appreciates lighter materials to decrease weight and improve fuel efficiency [2]. Lightweight oxides and carbides are considered as best reinforcements for MMCs, due to their high strength, low density, high Young's modulus and low chemical reaction [3]. In contrast to other metallic materials, magnesium (Mg) and its alloys can be used in the spacecraft and vehicle industries to support more fuel economy [4]. For the applications that require load bearing and strength, these lightweight materials are reinforced with high strength materials [5].

There have been several studies on the properties of Mg matrix composites, which demonstrated their higher strengths than single Mg alloys [6]. Numerous studies have demonstrated the biocompatibility and biodegradability of Mg-based materials, which have been employed for a wide range of orthopaedic applications, including nails, screws, splints, among others [7,27]. Materials formed from a matrix and reinforcements, commonly known

as MMCs, are important to determine the mechanical characteristics of their base metals [8]. The biodegradable MMCs have exhibited biodegradable properties along with properties, such as tensile, yield strengths and Young's modulus. Additionally, metal reinforcement has improved the composite resistant to corrosion [9,29]. Mg-based implants are becoming more popular with bone tissue applications. In the grain boundary, Mg composites are prone to micro galvanic corrosion and electrochemical stratification. Powder metallurgy (PM) is used to manufacture Mg-based MMCs with high hardness, wear resistance and low thermal expansion coefficient for aerospace, defence and automobile applications [10]. As a biodegradable material, Mg and its alloys are increasingly recognized and highly attractive for medical treatments. They offer similar mechanical properties to bone tissue, provide functional functions within human bodies and are highly biocompatible. They also have a better strength to weight ratio than most other metallic and polymeric biomaterials [11,31]. The shapes and features of their composite provide strength to their mechanical and constructional properties, thereby resulting to a wide range of engineering applications. In addition to features, such as low density, peak specific strength and good stiffness with measurement strength, Mg composites also provide excellent patterns for the creation of more advanced remote sensing products. When they are compared with monolithic alloys, Mg composites have greater wear resistance. In order to make Mg and its alloys more durable, composites have been developed with hard and rigid reinforcement [12,15,32,34,35]. However, physiological environments rapidly corrode Mg, causing it to lose several mechanical properties [9].

Moving forward, zinc oxide (ZnO) also possesses a number of physical properties, making it appropriate for use as organic materials [13]. As an element native to the human body, Zinc (Zn) can be processed and released from the body through metabolism, which makes it an ideal alloying element for biocompatibility. Humans need Zn for the synthesis of more than 300 enzymes and it is involved with the activities of more than these enzymes. The body suffers from a Zn deficiency in which deoxyribonucleic acid (DNA) replication is slowed; thus, limiting protein synthesis [14,31,33]. As one of the most important members of the metal oxide family, ZnO is an important material in terms of its mechanical, electrical and optical properties [15,28]. In recent decades, ZnO has been a highly studied semiconductor material, due to its unique optical, magnetic and electrical properties. Various morphologies and sizes of ZnO have been used in pharmaceutical creams, powders and dental pastes. ZnO is the best possible candidate to dope transition metals and rare earth metals, used to improve

the performance of ZnO devices and explore new applications. The use of ZnO for chemical additives has been demonstrated in various industries in addition to improving polymer properties [16]. Introducing a ZnO coating to the surface of whiskers during composite preparation produced an interfacial reaction, which built a strong interface for composites and provided an effective and feasible way to improve wettability [17].

Besides, powdered materials are pressed into a desired shape and then heated to fuse the powder together in a controlled atmosphere. PM is a constantly and rapidly changing technology, this includes a wide variety of metals and alloys, as well as a variety of shapes and sizes [18,30]. When compared with powder particles, PM has a higher level of production methods. As a result, it is considered to be a superior method for MMCs. The PM process involves blending of metal powders, compacting them and then sintering them at elevated temperatures. PM can be used to reduce the cost of manufacturing engineering components, as it is a proven and economical method. The use of PM in manufacturing increases the thermal conductivity, tribological behviour, seizure property and machinability property of products [19,20].

Yu et al. [1] reported that AZ91D composite reinforced with ternary Ti_2AlC MAX particles exhibited better properties than a composite reinforced with binary ceramic particles, such as TiC or ZnO. Witte et al. [5] described that the implants are temporarily required to provide mechanical support to the injured or pathological tissues during healing. Many authors have investigated Mg alloys as biodegradable biomaterials in recent years. Xie et al. [4] reviewed the metals and their alloy coatings were studied from the economic and utility perspectives. Turan et al. [8] investigated into the addition of carbon nanotubes (CNTs) to AZ31B Mg alloy, which influenced its properties. According to the results obtained, CNTs reduced corrosion resistance, because they formed galvanic cells with Mg. Bansal et al. [13] studied and considered Zn to be the most popular mineral in hard tissues. It is involved in numerous physiological functions of the immune system and aids cell growth in the AZ31 Mg alloy. It is also involved in numerous physiological functions of the immune system. Guan et al. [14] reported that addition of Zn to a matrix. The matrix became stronger through solution and aging strengthening. It also improved the electrical potential and corrosion resistance. Selvam et al. [15] investigated into ZnO nanoparticles reinforced Mg matrix composites by PM technique and observed an improved wear resistance with the ZnO-Mg composite.

Chaubey et al. [36] reported on the synthesis of Mg-7.4%Al bulk proposed composite, using hot pressing followed by hot extrusion process. The mechanical properties of the proposed composites were examined by using compressive strength. To examine the structure mechanism relation, the fracture surface after compression test was done to investigate the crack propagation implementation. Chaubey et al. [37] investigated into the microstructural development of the Mg-7.4%Al alloy by X-ray diffraction, scanning and transmission electron microscopies. Mg-7.4%Al powder was manufactured by using mechanical alloying with high-energy mill. The deviation of crystallite size and lattice strain were examined during milling process. Hardness of the powders was also evaluated as a function of milling time. Mg cores showed lower hardness of 40-50 HV and the Mg-Al combined regions displayed the higher hardness of 170 HV. Shadangi et al. [38] examined the PM process of AA 6082 Al matrix composite reinforced by non-equiatomic AlSiCrMnFeNiCu high-entropy alloy (HEA). The microstructure evolution and phase composition of Al-HEA powders were distinguished by scanning electron microscopy (SEM)/energy dispersive X-ray (EDX), X-ray diffraction (XRD) and transmission electron microscopy (TEM). Al-HEA nanocomposite powders were associated with the help of pressure-less sintering process at 560 °C. The microhardness of Al-HEA nanocomposites were measured in the series of ~ 0.90 to 1.81 GPa. The properties of the aluminium matrix composites (AMCs) can be personalized and improved by strengthening them with the suitable reinforcement particles. AMCs have presented an significant increase in HV, due to the uniform distribution of reinforcement particles and development of the transition layer at the boundary. Nandhini et al. [39] investigated into the equiatomic MgAlSiCrFe high-entropy alloy by using mechanical alloying process. The phase composition, phase evolution, alloying behavior and thermal strength of as-milled nanostructured powders of HEA were determined through XRD, TEM, SEM and differential scanning calorimetry (DSC). The nanocrystalline HEA powder was developed during milling with a crystallite size of 19 ± 0.8 nm. In the past three decades, significant efforts have been given to the growth of high-strength materials. This led to the innovation of quasicrystals, bulk metallic glasses and HEA. Shadangi et al. [40] studied the effect of Al–Cu–Fe (40 vol%) quasicrystalline (QC) reinforcement particle on the microstructure morphology and phase composition of AMCs manufactured by mechanical milling process and spark plasma sintering (SPS). The characterization of AMCs was analyzed through XRD, TEM and SEM. AMCs are conservatively strengthened with ceramic particle reinforcement, such as carbides, nitrides and oxides, having higher strength, modulus of elasticity and thermal stability.

Suguna et al. [41] analyzed the hexagonal phase ZnO nanostructures, using hydrothermal method with different temperatures: 200, 400, 600, 800 and 1000 °C. The XRD, Fourier Transform infrared spectroscopy (FTIR), field emission scanning electron microscopy (FE-SEM), high-resolution transmission electron microscopy (HR-TEM), ultra-violent-vis diffuse reflectance spectroscopy (UV-DRS) and X-ray photoelectron spectroscopy (XPS) techniques were characterized for the proposed nanostructures. The crystallite bulks of the proposed nanomaterials were measured by Williamson–Hall plots techniques. The ZnO strengthened at 200 °C displayed a crystallite size of 18.7 nm while the ZnO annealed at °C indicated a 46.2 nm. When increasing the annealing temperature, the crystallite sizes were improved, because of persuaded development of crystallites for the period of annealing procedure. Similarly, the band cracks of the ZnO annealed at different temperatures displayed a decreasing trend with increasing annealing temperatures. Prabhu et al. [42] manufactured the spindle-shaped ZnO and reduced graphene oxide sheets by using hydrothermal method. ZnO/r-GO composite was produced by direct solution mixing technique. Numerous characterization outcomes established the interior and exterior decoration of spindle-shaped ZnO on the reduced graphene oxide sheets. The surface states, optical properties, phase formation, morphology and crystalline structure were characterized by using UVeVis spectroscopy, TEM, XPS, FTIR, XRD and FESEM. Prabhu et al. [43] synthesized the well-defined dumbbell shaped ZnO by hydrothermal method and ZnO dumbbell/reduced graphene oxide (ZnO/rGO) nanocomposites were produced by a simple solution mixing method. The development of shape, nanocomposites, crystal structure, size and optical properties of the ZnO/rGO nanocomposites were examined by several analytical methods. Prabu et al. [44] produced the djembe like ZnO microstructure evolution by surfactant-assisted hydrothermal method and the composite with g-C_3N_4 was manufactured by an ethanolic reflux method. In addition to electrical, optical, morphological and their photocatalytic activities were examined. The photocatalytic presentation was examined by dye degradation test under visible light irradiation. Jayakrishnan et al. [45] manufactured the dumbbell-shaped ZnO nanostructure, using hydrothermal method through elevated hydrothermal temperature of 200 °C. The XRD displayed the development of the hexagonal crystalline structure with high-phase purity. XPS was used to analyze the chemical surface states. The ZnO nanostructured materials exhibited possible applications, as super capacitors and textile wastewater treatments.

Considering the afore-reported extensive literature, it was evident that several manufacturing processes have been used to support the relevance of ZnO and other particles

as reinforcements in Mg-based composites. Nevertheless, there was no reported study exactly on influences of ZnO addition on both microstructure and mechanical properties of sintered Mg matrix composites, specifically with variable ZnO filler contents of 0 to 9 weight percentage (wt.%) and PM technique. The main objective of this study was to synthesize Mg-3Al-xZnO (where x = 3, 6 and 9 wt.%). Therefore, the present work studied various Mg-3Al-ZnO composite samples, which were manufactured through PM technique. The microstructure, mechanical and corrosion properties of the proposed composites were analysed. The worn surfaces of the samples were thoroughly studied, using scanning electron microscopy (SEM). The suitable wear parameters were identified, based on signal-to-noise (S/N) ratio analysis. The contour and probability plots were provided for better understanding of the influences of wear parameters on their wear rate (WR) and coefficient of friction (COF). The optimal process parameters were obtained for the best composite sample.

2. Experimental details

Fig. 1(a) depicts the PM process used to fabricate the Mg-3wt.%Al-ZnO composites. Figs 1(b-d) show the images of Mg, Al and ZnO powders used in this work and fabricated composite samples: Mg-3wt.%Al, Mg-3wt.%Al-3wt.%ZnO, Mg-3wt.%Al-6wt.%ZnO and Mg-3wt.%Al-9wt.%ZnO. The powders were received from Kemphasol, Mumbai, India. The Mg powders were 99% pure and possessed a particle size of <200 μm. To prepare the composite mixtures, certain measured amounts of powder were ball milled in a planetary mill at a speed of 120 rpm for 3 hours with the ball-to-powder ratio of 10:1.

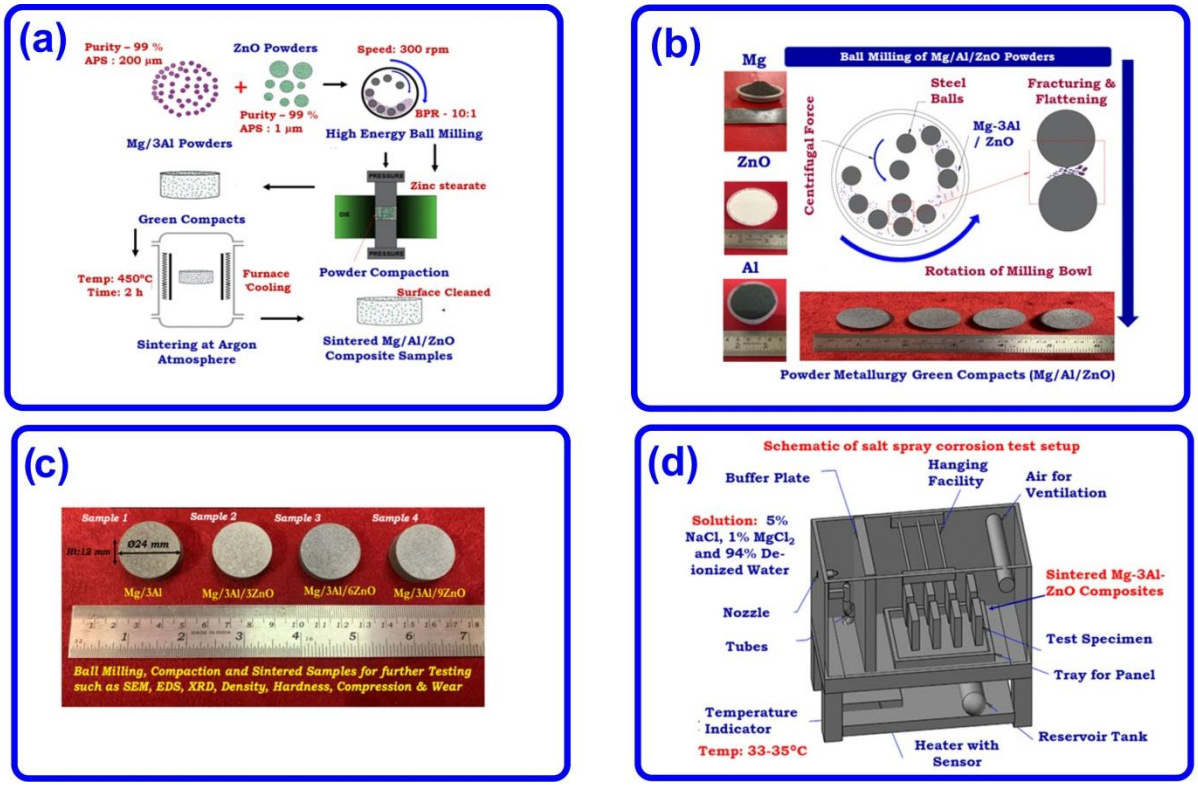

Fig. 1. (a) Schematic of PM process for Mg-3Al-ZnO composite, (b) images of Mg, Al and ZnO powders as well as the fabricated composite samples, (c) sintered samples of the various composites used and (d) schematic of salt spray corrosion test setup.

The ball milled powders were compacted, using a hydraulic press (Model: Universal Tun-400) with height of 12 mm and diameter of 24 mm. Zinc stearate was used as a binder to ease compact ejection. Green compacts were sintered in a high temperature. Argon furnace (Model: Hi-Tech 1200 ^{o}C) with a vaccum pump was used for 2 hours at 450 ^{o}C at a rate of 10 °C/min to complete the compacting process. Magnesium melted around 650 ^{o}C. During powder metallurgy process, sintering temperature was considered as 60-70% of the melting point of the alloy. Therefore, 450 ^{o}C was between the sintering range, where the process was carried out for 2 hours. Azaath et al. [48] synthesized PM copper –SiC composites in argon atmosphere tubular furnace, where the hold or soaking period was only 30 minutes, which was much less than the present investigation. Samples were cooled in the furnace during the sintering process. The sintered composites were cleaned with emery sheets and then polished with a polishing machine before testing. Fig. 1(c) shows the sintered samples of Mg-3wt.%Al, Mg-3wt.%Al-3wt.%ZnO, Mg-3wt.%Al-6wt.%ZnO and Mg-3wt.%Al-9wt.%ZnO.

By employing Archimedes' principle, the densities of the Mg-3wt.% Al alloy and its composites were determined [46]. Based on the Archimedes' principle, a density measuring kit was used to calculate the density of the sample. The rule of mixture was used to calculate the theoretical density, experimental density and % of porosity. A weighing balance with a precision of 0.0001 g was used to record the weights of each sample. This method was adopted based on the previous investigation on synthesis of Mg-3wt.%Al-ZnO composites and Mg-3wt.%Al samples [49].

In this study, the theoretical densities of the ball-milled Mg alloy and its composites were calculated, using the densities of Mg, Al and ZnO. In addition, SEM (Make-EVO-18, Carl Zeiss) and energy dispersive spectroscopy (EDS) (Make-TESCAN VEGA3-Wsource) were used for the evaluation of the morphology of the ball milled Mg alloy and its composites. The proposed composites were analyzed, using SEM for composition and microstructure. Fig. 2(b) shows the SEM images of the Mg and ZnO. X-ray diffraction (XRD) measurements were carried out, using Malvern Panalytical X Pert^{3}Powder System with a Cu-K α (λ = 1.54060A°) operated at 20 mA and 40 kV for ball milled composite powders and sintered composite samples. Fig 3 depicts the XRD pattern of as-received ZnO powder. The XRD patterns of Mg-3Al powders were reported in our previous publication [47]. Al powder XRD was not provided, due to the presence a matrix with a lower weight percentage of 3, the Al peak was not apparent in the XRD pattern. The integration of low weight percentages of reinforcement elements. Generally, if the presence of any element is less than 5 wt.%, it cannot be detected by XRD [54].

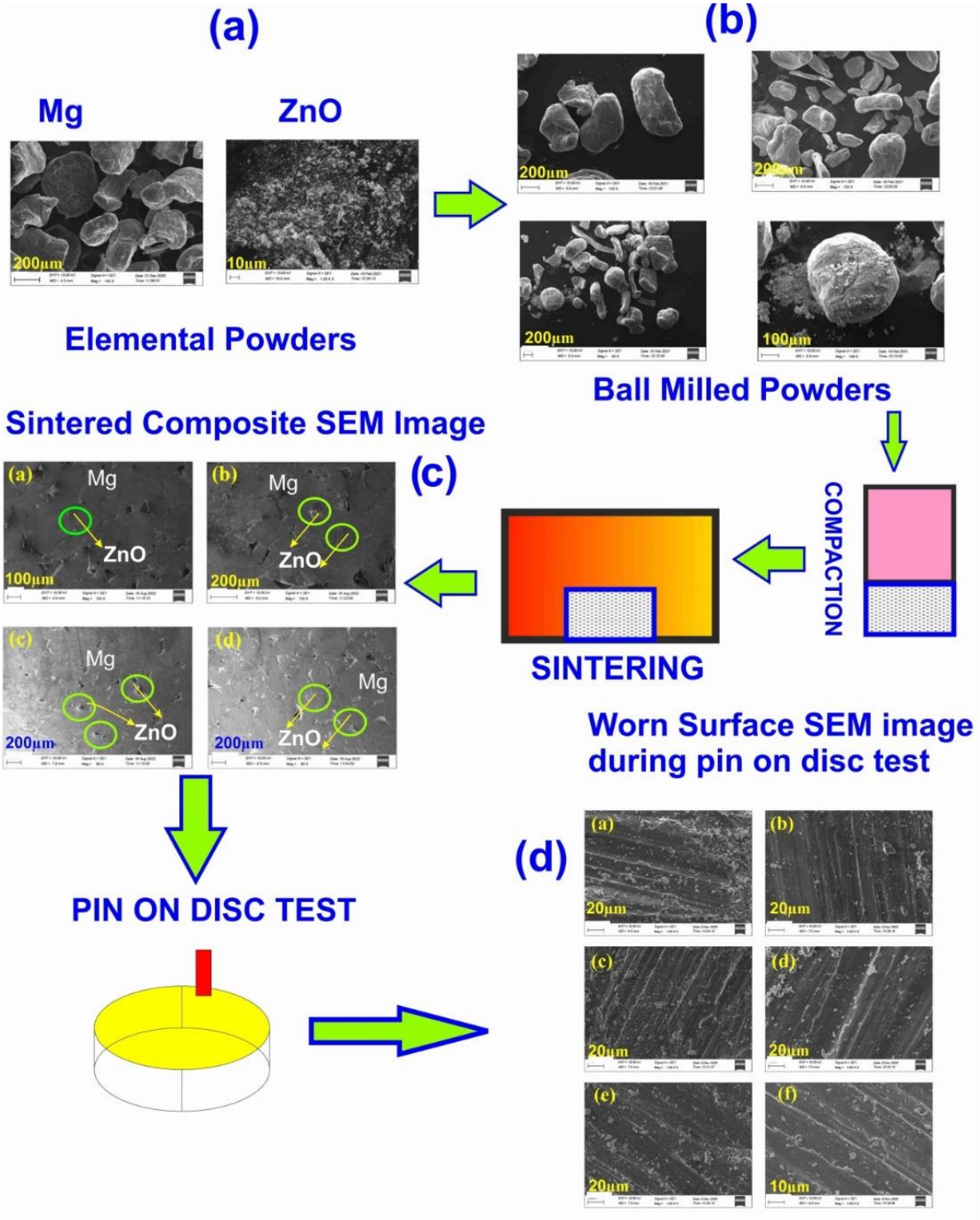

Fig. 2. (a) SEM images of as-received Mg and ZnO powders,

2 (b) SEM images of ball milled Mg-3Al-ZnO composite powders, showing (a) Mg-3wt.%Al-3wt.%ZnO, (b) Mg-3wt.%Al-6wt.%ZnO, (c) & (d) Mg-3wt.%Al-9wt.%ZnO.

2 (c) SEM images of sintered Mg-3Al-ZnO composites, showing (a, b) Mg-3wt.%Al-3wt.%ZnO, (c) Mg-3wt.%Al-6wt.%ZnO and (d) Mg-3wt.%Al-9wt.%ZnO.

2 (d) Worn surface images of sintered Mg-3Al-ZnO composites, showing (a, b) Mg-3wt.%Al-3wt.%ZnO, (c, d) Mg-3wt.%Al-6wt.%ZnO and (e, f) Mg-3wt.%Al-9wt.%ZnO.

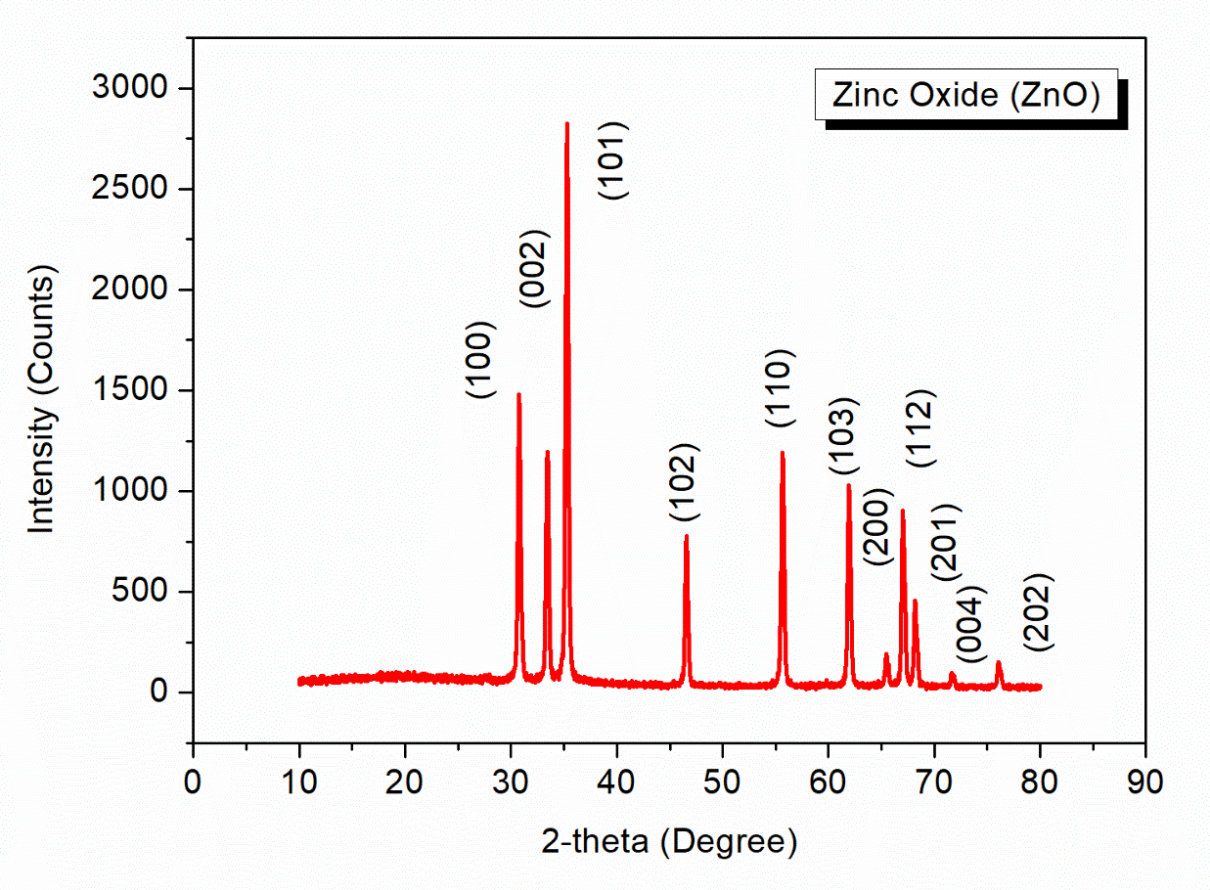

Fig. 3. XRD pattern of ZnO powder.

Hardness tests were conducted on sintered composite samples according to the E-384 ASTM standard with an automatic digital micro hardness tester (Model: Holmarc MV1-PC) under 1 Kg of load and 15 seconds of dwell time. An average value was taken for the hardness based on the results obtained from five locations on each of the samples. More also, the compressive strengths (CS) of the sintered composites were determined in accordance with ASTM E-9 standard, using an ASTM-approved universal testing machine (Model: M-50) with a 50 kN capacity and crosshead speed of 3 mm/min.

In accordance with ASTM B-117 (corrosion tests under artificial atmospheres - salt spray tests), corrosion tests were conducted using salt spray. A 5% sodium chloride, 1% magnesium chloride and 94% de-ionized water solution with temperature of 33-35 ^{o}C and relative humidity of 98% were used in 1.0 litre of solution at relative humidity of 98%. Each sample was weighed after eight hours, a buffer solution was added and a pH of 7.5

maintained. Fig. 1(d) shows the schematic of salt spray corrosion test setup. Continuous air was atomized at 2 to 3 bars, using pressure regulation. Following each weight measurement, the corrosion rate was calculated on the horizontal surface area of the experiments, which was 12 cm^2. The experiment was tilted at 45^o to the plumb line.

Furthermore, pin-on-disc setup (Make: Ducom Wear test) was used to determine their wear rate (WR) and coefficient of friction (COF). The pin-on-disc test involved inserting an elbow-shaped pin perpendicularly into the circular counter plate. By using a lever and weight, the specimen was pressed against a rotating disc at a given load. The disc was also rotated at a specified speed. The quantity of wear was determined by weighing the pin before and after the test. During this experiment, specimens with a diameter of 10 mm and a length of 30 mm was used, as similarly reported [21]. Test was conducted according to the ASTM G99 standard. The thickness and diameter of the hardened steel disc were 8 and 165 mm, respectively. Weight difference method was used to determine loss of wear. The friction force was measured with friction sensors. The friction coefficients were later calculated by measuring the friction force. The experimental design used was based on Taguchi L_{16} orthogonal array, as similarly employed [24]. Detailed information on parameters, levels and experimental details are presented in Tables 1 and 2. Both Eqs (1) and (2) were used to determine the value of WR.

$$WR = \frac{Mass\ loss\ x\ Density}{D}\ (mm^3/m) \quad (1)$$

$$V = \frac{\pi DN}{1000} \quad (2)$$

Eq. (2) Where V = Velocity (m/min), D = diameter (mm) and N = speed (rpm).

Table 1

Parameters and levels.

Wt.% of ZnO	0	3	6	9
Applied load, P (N)	5	10	15	20
Sliding distance, D (m)	500	1000	1500	2000
Sliding velocity, V (m/s)	1	2	3	4

Table 2

Experimental details.

Exp. Number	Wt.% of ZnO	P (N)	D (m)	V (m/s)	WR (mm^3/m)	COF	S/N ratio WR	Mean WR	S/N ratio COF	Mean COF
1	0	5	500	1	5.861	0.55	-15.3594	5.861	5.192746	0.55
2	0	10	1000	2	6.247	0.52	-15.9134	6.247	5.679933	0.52
3	0	15	1500	3	7.864	0.56	-17.9129	7.864	5.036239	0.56
4	0	20	2000	4	11.697	0.63	-21.3615	11.697	4.013189	0.63
5	3	5	1000	3	5.247	0.30	-14.3982	5.247	10.45757	0.30
6	3	10	500	4	6.278	0.46	-15.9564	6.278	6.744843	0.46
7	3	15	2000	1	6.957	0.50	-16.8484	6.957	6.020600	0.50
8	3	20	1500	2	9.361	0.61	-19.4264	9.361	4.293403	0.61
9	6	5	1500	4	6.934	0.44	-16.8197	6.934	7.130946	0.44
10	6	10	2000	3	7.348	0.49	-17.3234	7.348	6.196078	0.49
11	6	15	500	2	7.869	0.52	-17.9184	7.869	5.679933	0.52
12	6	20	1000	1	8.624	0.59	-18.7142	8.624	4.582960	0.59
13	9	5	2000	2	3.215	0.39	-10.1436	3.215	8.178708	0.39
14	9	10	1500	1	3.694	0.41	-11.3499	3.694	7.744323	0.41
15	9	15	1000	4	3.785	0.46	-11.5613	3.785	6.744843	0.46
16	9	20	500	3	4.128	0.48	-12.3148	4.128	6.375175	0.48

3. Results and discussion

3.1 Characterization analysis of composite powders

Previously, Fig. 2(b) depicts the SEM images of ball milled Mg-3Al-ZnO composite powders. The ZnO particles were evenly distributed within the Mg alloy matrix. As observed, the ZnO particles were not agglomerated in the Mg alloy matrix. This can be attributed to proper powder milling process. The presence of more ZnO content was observed in Figs 7(c) and (d) for the Mg-3wt.%Al-9wt.%ZnO composite sample. According to the SEM analysis, the ZnO powders were smaller than the matrix particles of Mg. The compaction process was followed after ball milling process. The ZnO powder size was reduced after ball milling process. The size of ZnO was lower than size of Mg, therefore ZnO entrapped between the spaces of Mg during the compaction process. Reinforcing

particles were also measured by their size and shape to determine the required properties of the composites [15,23].

The planes of both matrix and reinforcement can be observed by examining the XRD patterns. Therefore, Fig. 4 shows the XRD patterns obtained from the milled Mg-3wt.%Al-ZnO powders. Mg recorded the higher peak in all of the patterns and ZnO produced the lower peak, because ZnO was at a lower concentration than Mg. Adding ZnO to the Mg-3wt.% Al alloy matrix reduced the peak intensity of Mg in the composite. ZnO was well incorporated into the Mg matrix, as evident from the XRD patterns of the composite powders. Additionally, it was significantly observed that there were no other compounds formed in the high energy ball milling process, similar to the earlier reported results. ZnO peak of XRD patterns were recognized and indexed based on reported patterns: JCPDS No. 36-1451. The 2θ plotting is merely practical, because many machines use fixed sources, which results to a measured detector angle of 2θ with respect to the incident beam. As the detection circuit typically counts the number of pulses (related to the number of detected photons), "counts" is the most widely used unit of measurement. Of course, choosing time at arbitrarily and graphing it in "counts" would not give an absolute scaling.

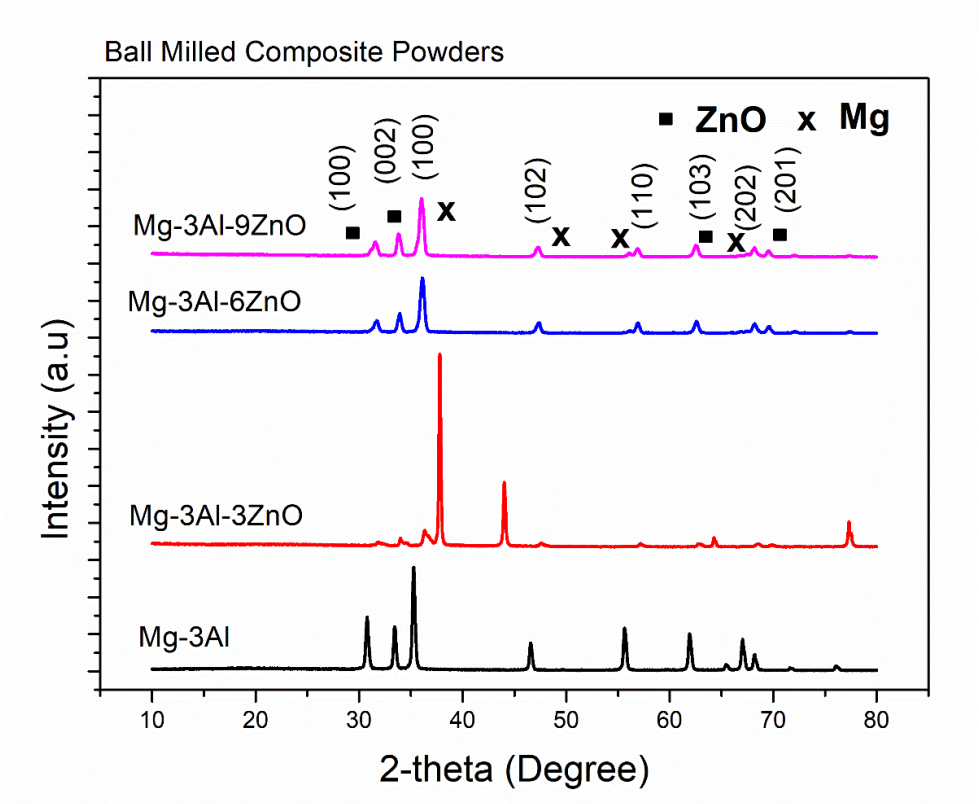

Fig. 4. XRD patterns for Mg-3wt.%Al-ZnO composite powders.

More also, Fig. 5 shows the XRD patterns obtained from the Mg-3wt.%Al alloy and Mg-3wt.%Al-ZnO composites sintered at 450 ^{o}C. There were many peaks recorded in all compositions of the synthesised composites, corresponding to Mg. The peak formed at 36 degrees adjoining to Mg peak was confirmed as ZnO. The Al peak in the XRD structure appeared to be less noticeable, because of its low content of 3 wt.% used in the matrix.

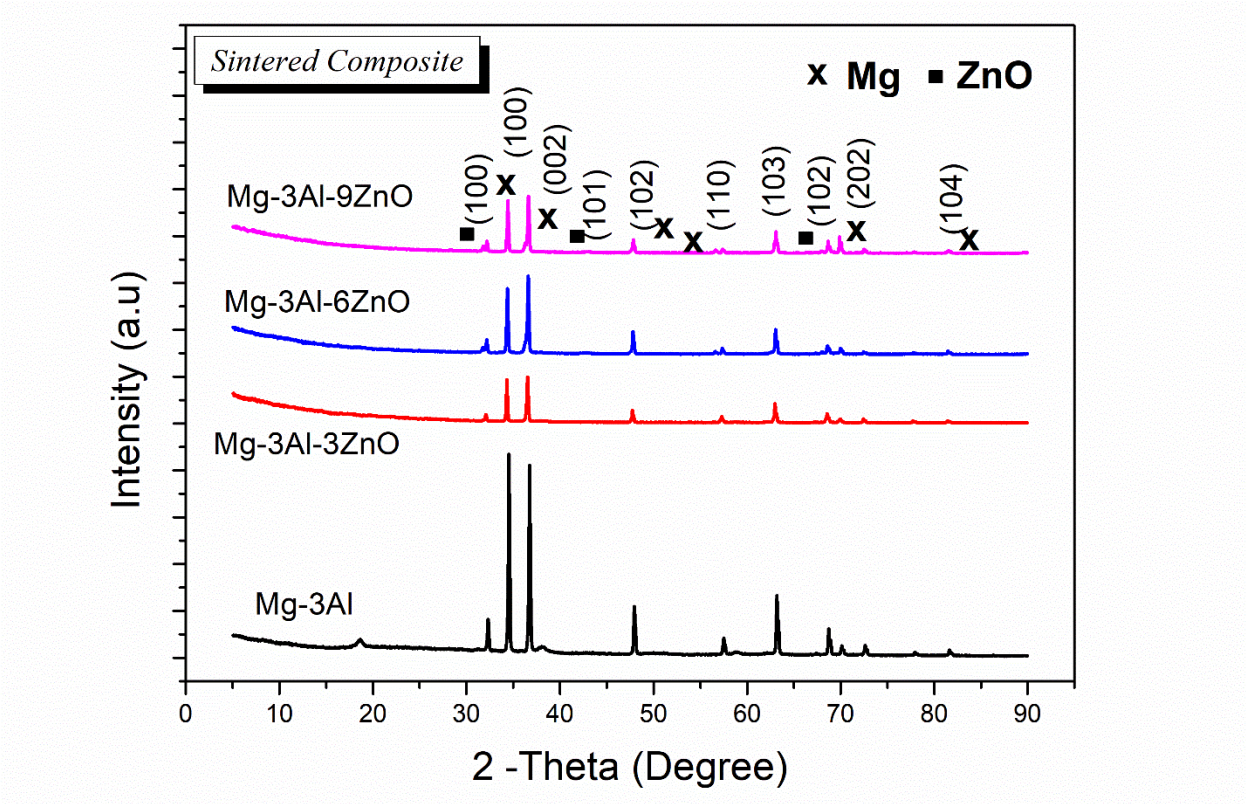

Fig. 5. XRD patterns for Mg-3Al-ZnO sintered composite samples.

The SEM images of the sintered Mg-3Al-ZnO composites have been previously shown in Fig. 2(c). Among all the images obtained, the ZnO particle was evenly distributed across the matrix. There was a better adhesion between the ZnO particle and Mg matrix, as observed from all the samples. There was no agglomeration observed on the samples with more wt.% of ZnO. Due to the ball milling process, a uniform distribution was achieved among Mg, Al and ZnO powders. During the milling process, the size of ZnO was reduced, because the milling process was effective. Fracture of reinforcement was caused by the impact of the balls and particles on the reinforcements during milling operation [22].

Figs 6 (a)-(d) show the energy dispersive X-ray (EDX) images of Mg-3wt.%Al alloy and its ZnO reinforced composites. Fig. 6 (a) depicts the Mg-3wt.% Al alloy, the Mg peak was significantly observed from the plot. Figs 6 (b)-(d) show the EDX of the composite samples and their respective ZnO and Mg peaks. Al peak was observed in Figs 6 (b) and (d), and

weight and atomic percentages are provided in all the images. During the sintering process and at the same instance, vacuum was applied before the sintering. Therefore, oxide formation during sintering was very small. The same phenomena of presence of oxygen has been previously observed and reported in EDS results of synthesised Ni-10Co-5Cr, using PM [52].

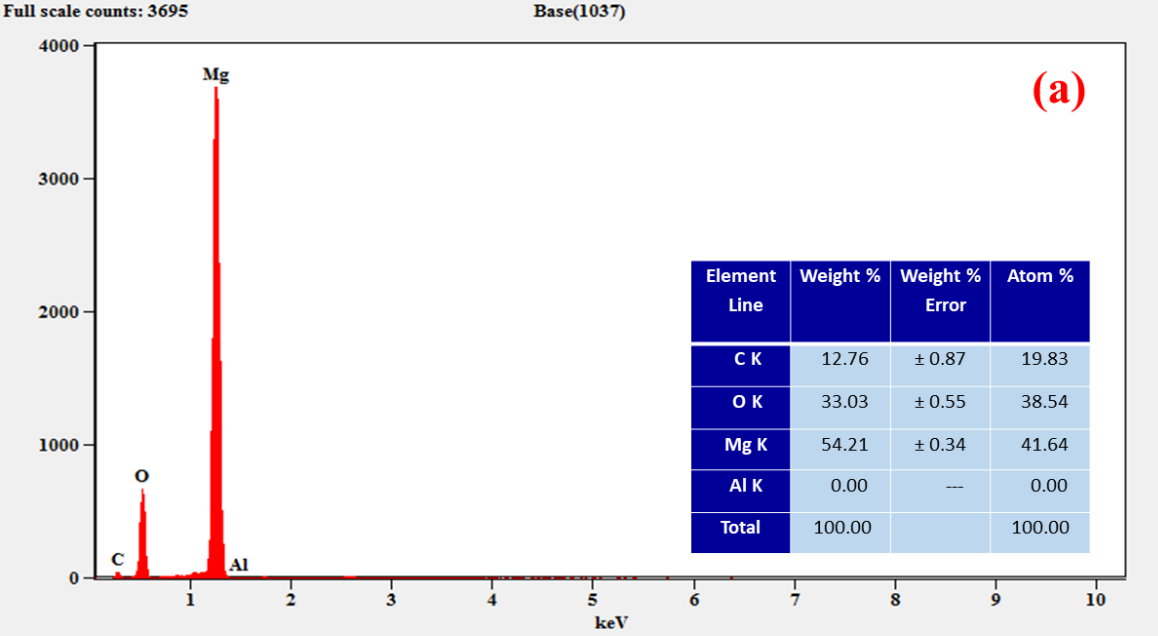

Element Line	Weight %	Weight % Error	Atom %
C K	12.76	± 0.87	19.83
O K	33.03	± 0.55	38.54
Mg K	54.21	± 0.34	41.64
Al K	0.00	---	0.00
Total	100.00		100.00

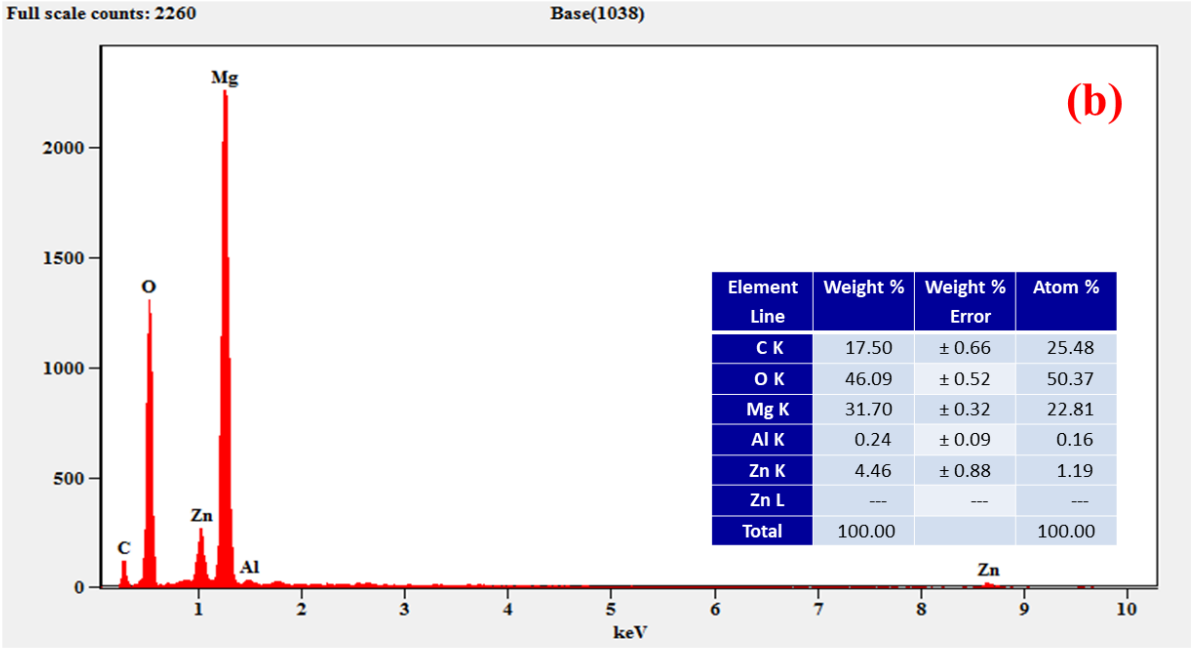

Element Line	Weight %	Weight % Error	Atom %
C K	17.50	± 0.66	25.48
O K	46.09	± 0.52	50.37
Mg K	31.70	± 0.32	22.81
Al K	0.24	± 0.09	0.16
Zn K	4.46	± 0.88	1.19
Zn L	---	---	---
Total	100.00		100.00

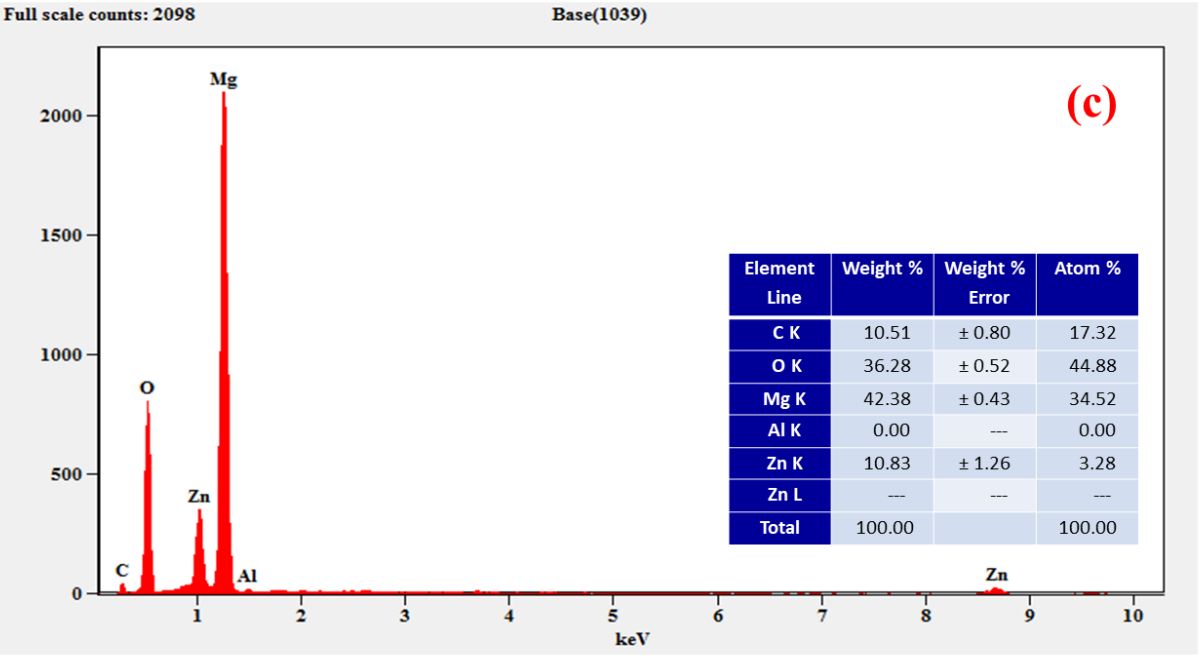

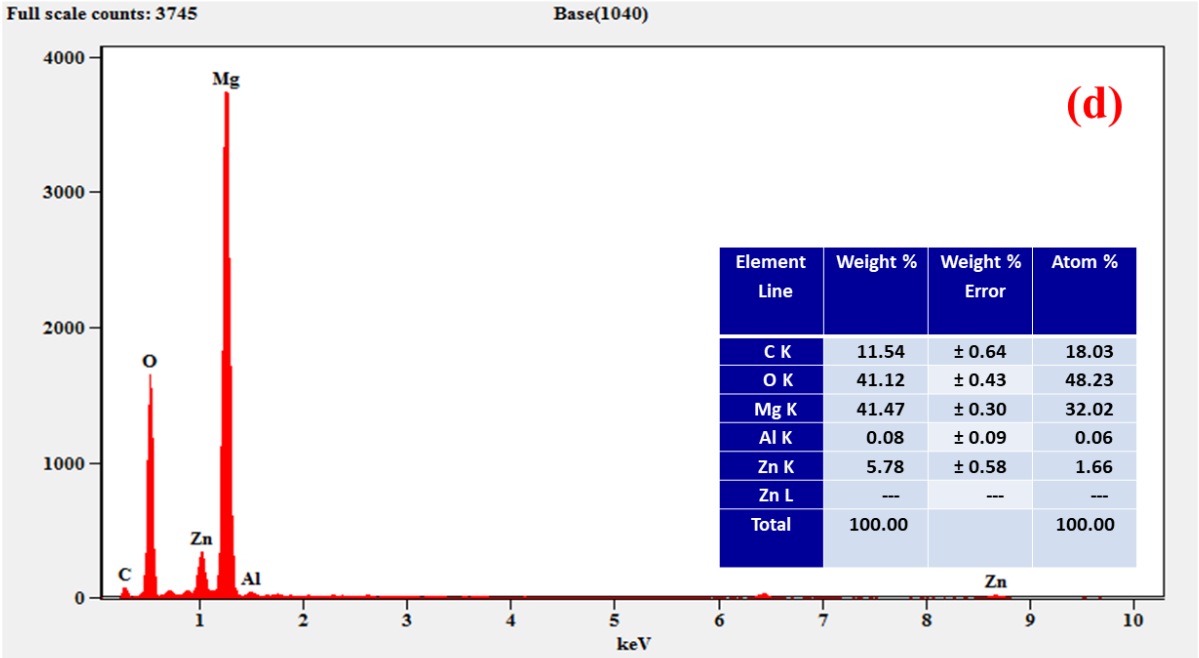

Fig. 6. EDX of sintered Mg-3Al-ZnO composites (a) Mg-3wt.%Al-0wt.%ZnO (b) Mg-3wt.%Al-3wt.%ZnO, (c) Mg-3wt.%Al-6wt.%ZnO and (d) Mg-3wt.%Al-9wt.%ZnO.

Fig. 7 shows the effects of ZnO inclusion on the densities of Mg-3Al-ZnO composites. The density of the experimental sample increased with wt.% of ZnO in Mg alloy matrix. Each sample has a theoretical density that was greater than the experimental density. Similarly, the

porosity of the sample increased with the ZnO content in the matrix of Mg-3wt.%Al. Particles were effectively bonded together and voids were eliminated during the sintering process, which resulted to a higher density of sintered samples. Consequently, the sintered samples were denser than the green composite samples. The moisture from the samples was also removed during the heating process. The theoretical density is defined as the ratio of mass of sintered compact to the volume of the sintered compact. The experimental density is the density of sintered specimen which has low pore formation. The density of ZnO was higher than the density of magnesium, therefore the density increased with an increase in inclusion of ZnO. Due to the diffusion, sintered sample possess was higher density than green compact density. Eq. (3) was used for the porosity calculation.

$$Porosity = \frac{[(\rho_{Theoretical} - \rho_{Experimental})]}{\rho_{Theoretical}} \, x \, 100 \qquad (3)$$

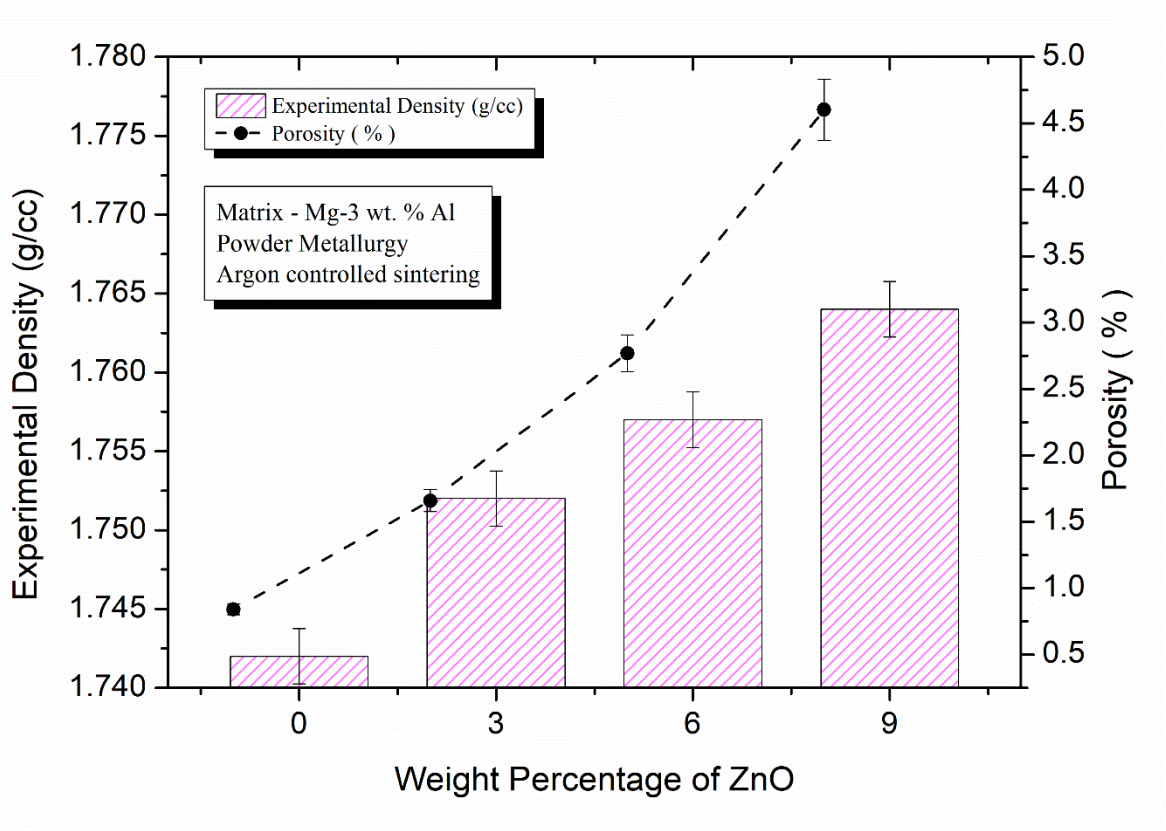

Fig. 7. Effects of ZnO on the densities of the various samples.

Fig. 8(A) depicts the indentation marks on (a) Mg-3wt.%Al, (b) Mg-3wt.%Al-3wt.% ZnO, (c) Mg-3wt.%Al-6wt.% ZnO, (d) Mg-3wt.%Al-9wt.% ZnO and Fig. 8(B) shows the influence of ZnO particle on the hardness property of Mg-3wt.%Al alloy matrix. By carefully examining the bar graph, it can be observed that the addition of ZnO to the Mg-3wt.% Al

alloyed matrix increased the hardness of the composite material. The hardness of ZnO particles was higher than the base Mg matrix. Therefore, it was easier to improve its hardness when a hard and suitable particle was added to a soft Mg matrix. Composites with ZnO content of 9 wt.% recorded the highest hardness, whereas base matrix alloys recorded the lowest hardness. It depends on many factors to achieve increased hardness, such as refined microstructures, the presence of secondary particles and uniform distribution of secondary particles. Those samples of Mg with over 9 wt.% of ZnO produced poor mechanical property, hence they were not reported. In addition, the results were ranged downward, due to the increased reinforcement of ZnO. Therefore, the threshold value of ZnO was 9 wt.% and it is not advisable to increase it more than this value.

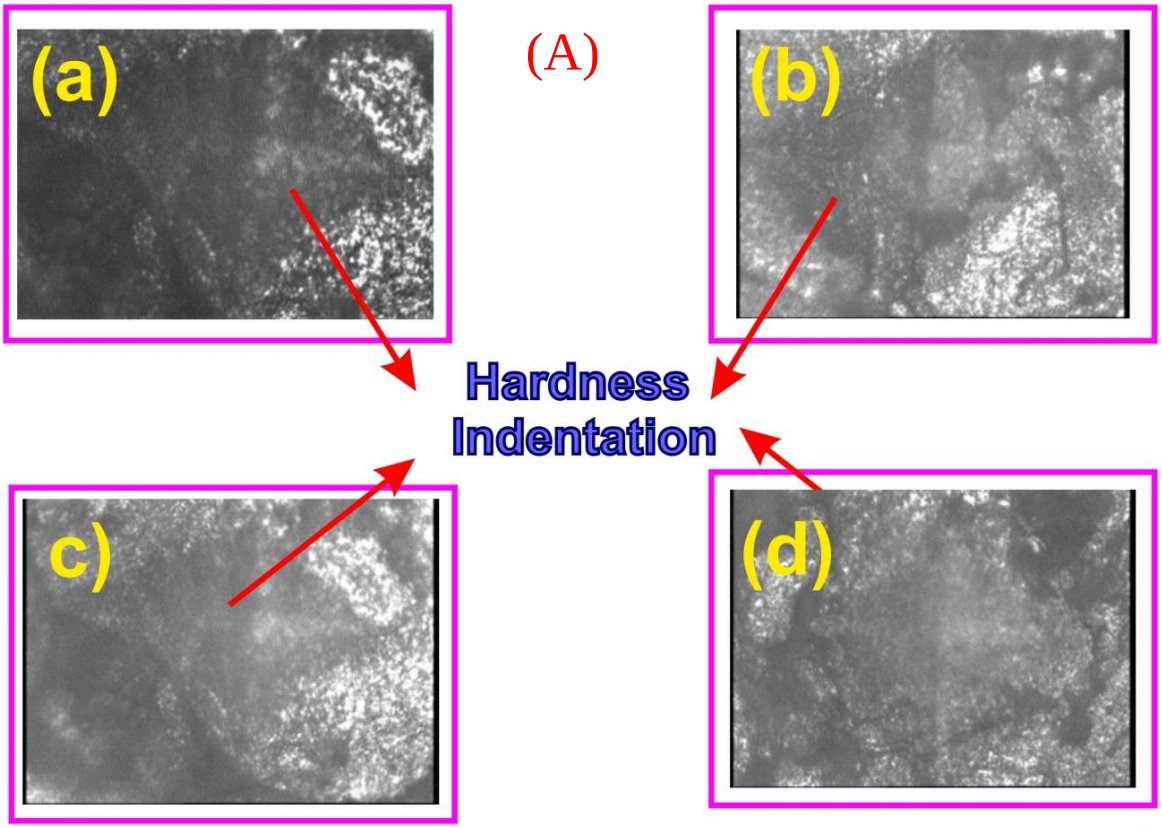

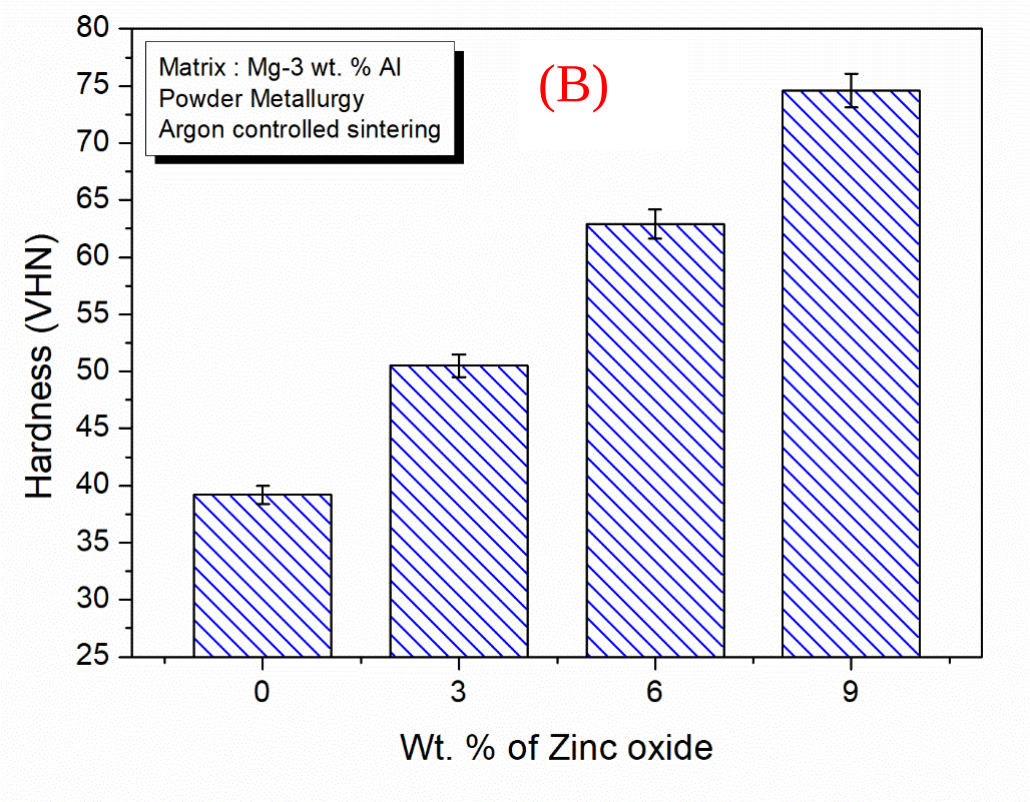

Fig. 8. (A) Indentation marks: (a) Mg-3wt.%Al, (b) Mg-3wt.%Al-3wt.% ZnO, (c) Mg-3wt.%Al-6wt.% ZnO, (d) Mg-3wt.%Al-9wt.% ZnO and (B) effects of ZnO on the hardness values of the various samples.

Fig. 9(a) shows the stress/strain plots obtained for the samples tested under compression load. Fig. 9(b) depicts the CS and elongation of the Mg-3wt.%Al and Mg-3Al-ZnO composites. A higher CS resulted from an increasing ZnO content in the matrix of Mg-3wt.%Al. Another possible explanation is the decreased elongation of the composite sample, as a result of the presence of rigid particles in the Mg-3wt.%Al matrix. As a result, the ductility decreased and the hardness of the composite increased. In order to improve the CS, ZnO particles in the matrix must be evenly distributed and properly bonded with the Mg matrix. CS was highest in the Mg-3wt.%Al-9wt.%ZnO composite sample, while the Mg-3wt.%Al alloy sample recorded a relatively low CS. The ZnO peak ensured a stable connection between Mg and ZnO. The strength of the composite was increased by incorporating ZnO to the matrix. It was observed that ductility decreased when ZnO content was increased. This can be attributed to the following reasons: (i) irregular interfacial bonding strength in the middle of the fillers and matrix material and (ii) irregular allotment of fillers with matrix and poor plasticity. Therefore, there was a decrease in elongation, similar to a previous study [53].

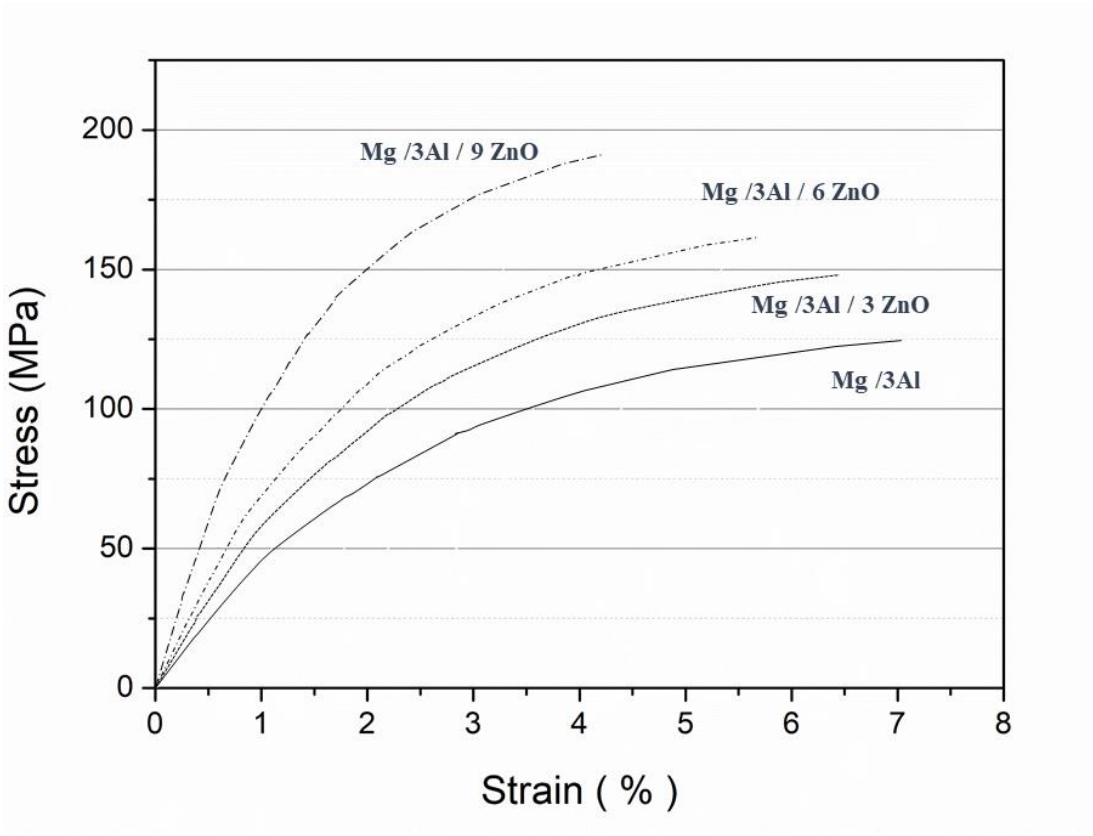

(a)

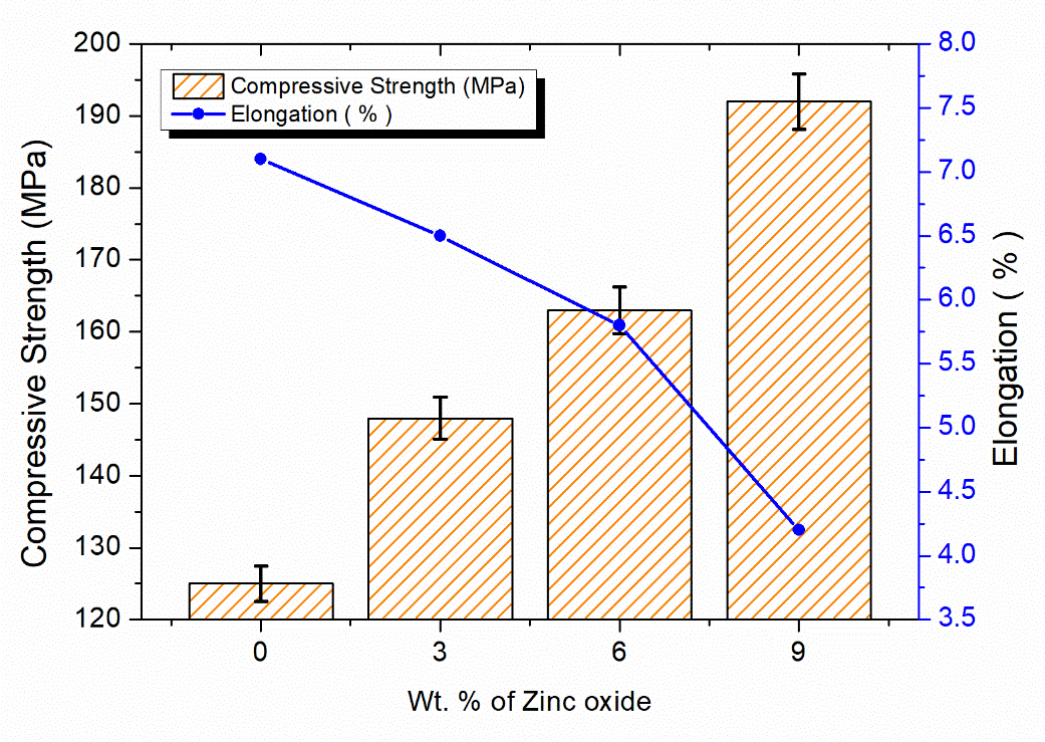

(b)

Fig. 9. (a) Stress/strain plots and (b) effects of ZnO on the CS and elongations of the various samples.

Fig. 10(a) shows the effects of ZnO on the corrosion behaviors of the various samples. The corrosion rate (mm/year) and weight loss of the Mg-3wt.%Al alloy and Mg-3Al-ZnO composite are presented in Fig. 10. According to the plot, the addition of ZnO to the Mg-3wt.%Al alloy in the salt spray test reduced the weight loss. Consequently, the corrosion rate (mm/year) also decreased with an increase in the amount of ZnO in Mg-3wt.%Al matrix. This indicated an improved corrosion resistance in the composites [14]. In this case, ZnO was spread appropriately in the grain boundary of the matrix. It also created a passive layer of protection for the surface against corrosion. Mg-based alloys are very relevant to biomedical applications. However, it is prone to corrosion in the presence of chloride ion. When oxide particle was added to the matrix, the corrosion resistance of the Mg alloy was enhanced. Therefore, heterogeneous microstructure of the composite contributed to its enhanced corrosion resistance [19]. The low corrosion rate observed from the samples with 9 wt.% of ZnO was 0.00158 mm/year, while Mg-3wt.%Al alloy exhibited the higher corrosion rate of 0.00374 mm/year. Fig. 10(b) depicts the corroded SEM images of Mg/3Al alloy and Mg/3Al/ZnO composites. The corroded surface evidently showed that the composite samples exhibited less corroded spots, when compared with unreinforced Mg/3Al alloy sample.

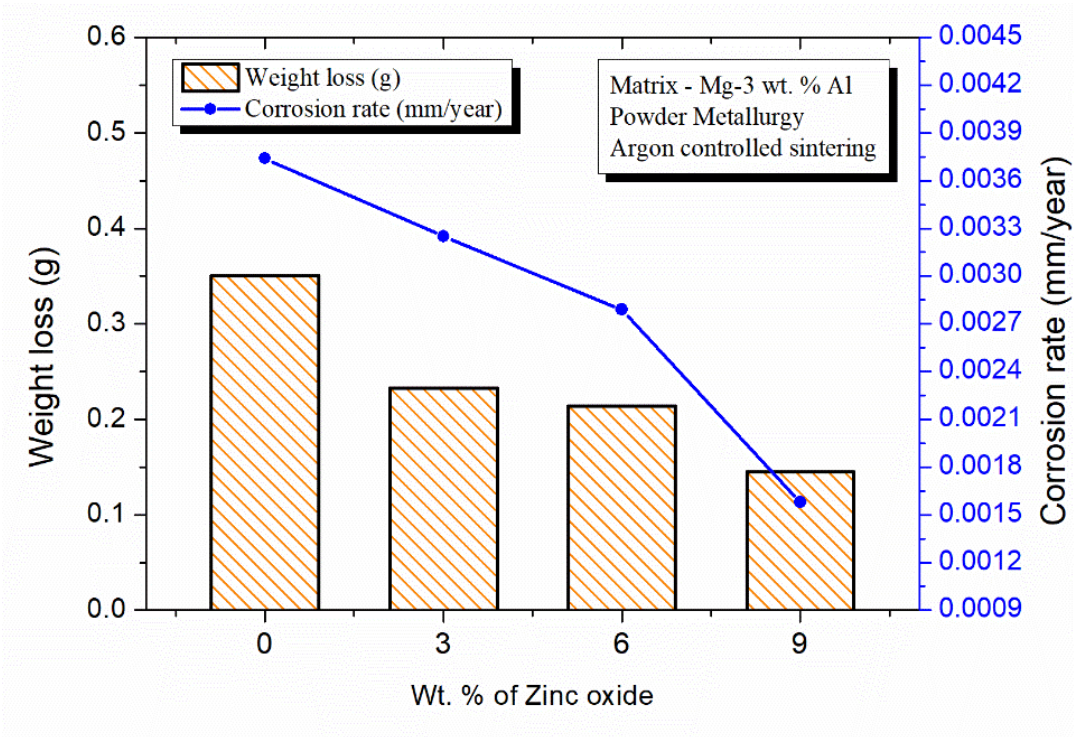

(a)

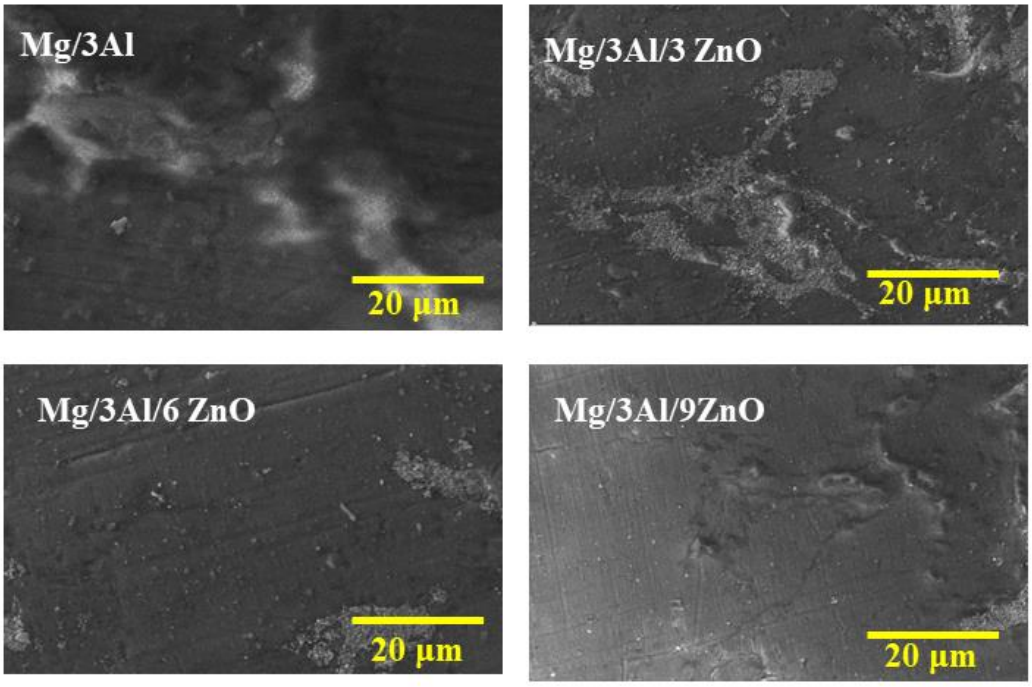

(b)

Fig. 10. (a) Effects of ZnO on the corrosion behaviors of the various samples and (b) corroded SEM images of Mg/3Al alloy and Mg/3Al/ZnO composites.

3.2 Analysis of variance

Analysis of variance (ANOVA) was used to analyze the effects of parameter combinations on the responses. A significance level of 5%; 95% confidence level was used for the response optimization study [22,23]. The COF values increased when the loading was high and the sliding speed was low. Localized welding on the sliding surfaces was responsible for the higher COF values. COF values were higher for sliding surfaces when loaded more, as they are more localized [24].

3.2.1 S/N ratio of analysis

Figs 11 and 12 depict S/N ratio and the mean plots for the WR, respectively. For the most WR, it was observed that the reinforcement levels of $A_4B_1C_2D_3$ were better at Level IV (9 wt.%), P at Level I (5 N), D at Level II (1000 m) and V at Level III (3 m/s). Fig. 13 shows the S/N ratio plot of COF. Fig. 14 depicts the mean plot for the COF. From the analysis, it was evident that the combined parameters of $A_4B_1C_2D_3$ produced the optimum COF. It represented the reinforcement at Level IV (9 wt.%), P for level I (5 N), D for level II (1000 m) and V for level III (3 m/s).

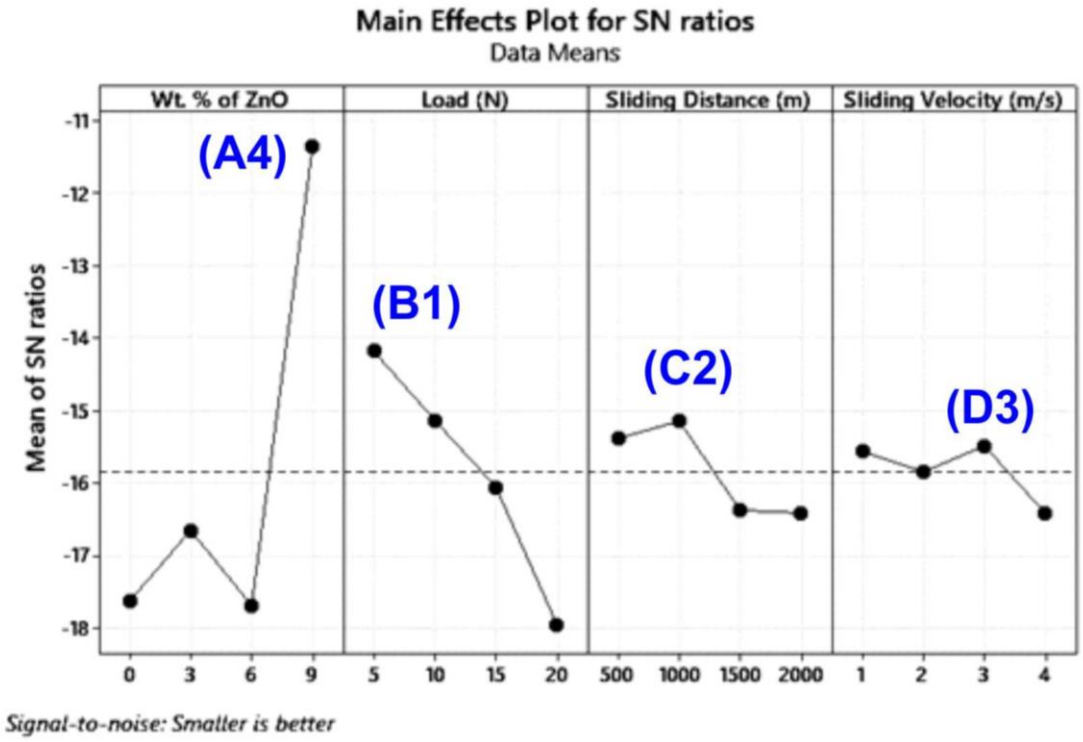

Fig. 11. S/N ratio plot of WR obtained from the Taguchi analysis for various input parameters wt.% of ZnO, L, D and V.

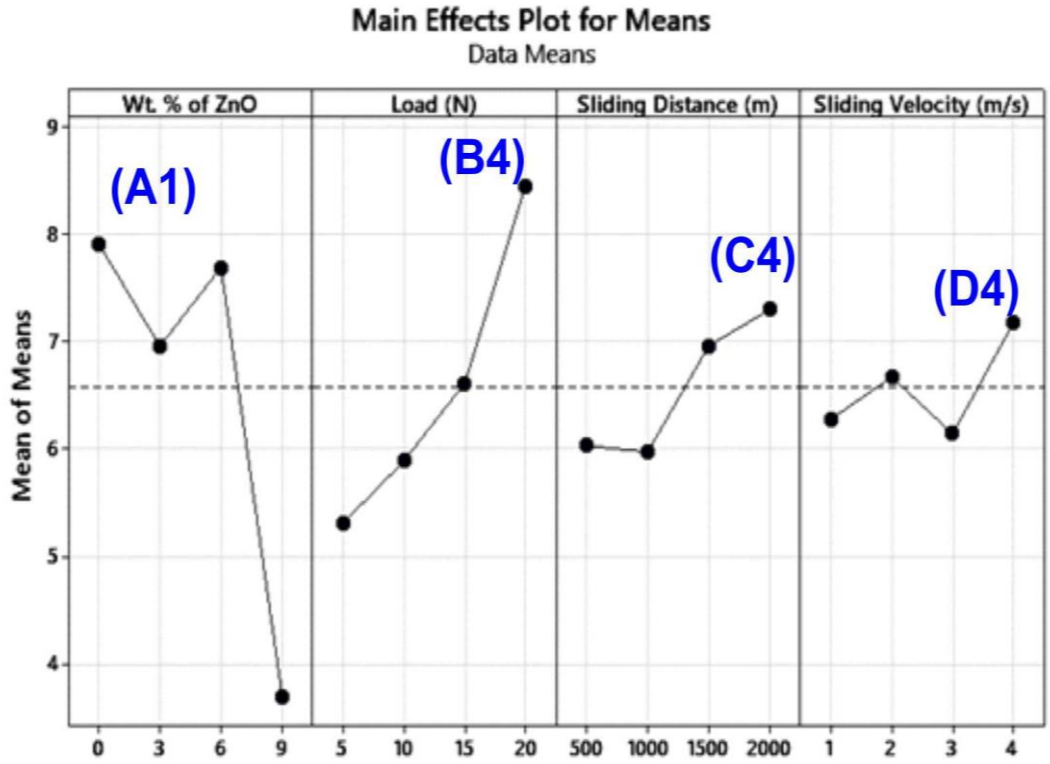

Fig. 12. Means plot of WR obtained from the Taguchi analysis for various input parameters wt.% of ZnO, L, D and V.

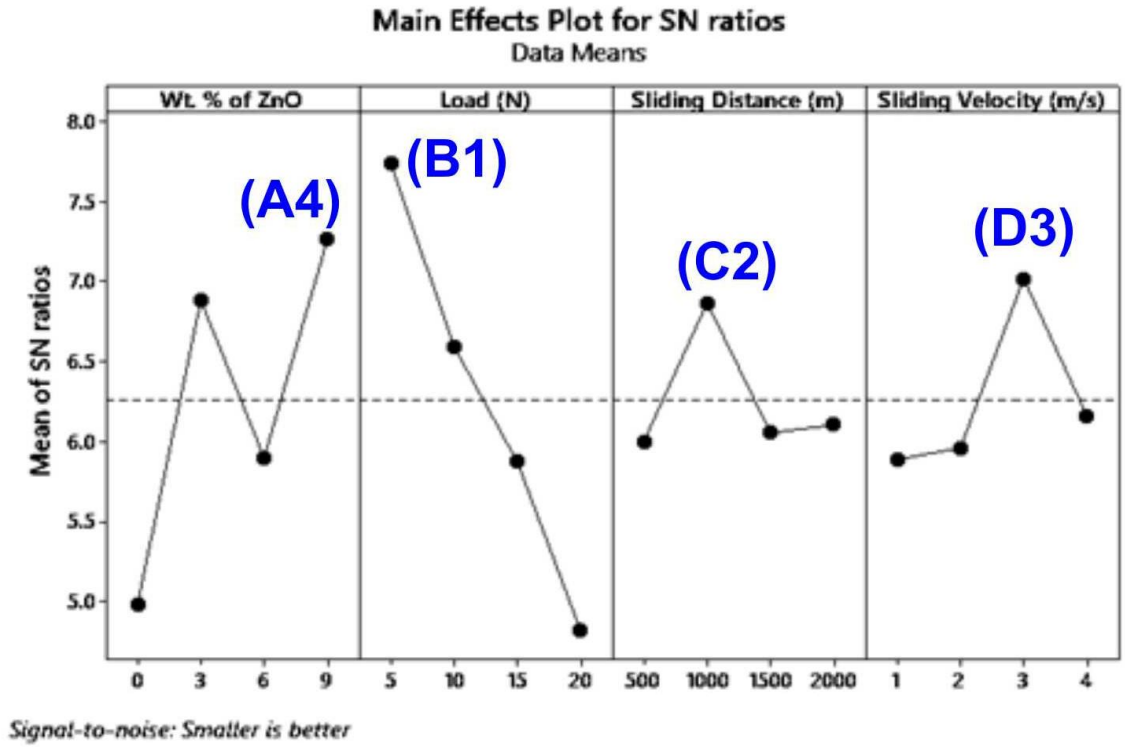

Fig. 13. S/N ratio plot of COF obtained from the Taguchi analysis for various input parameters wt.% of ZnO, L, D and V.

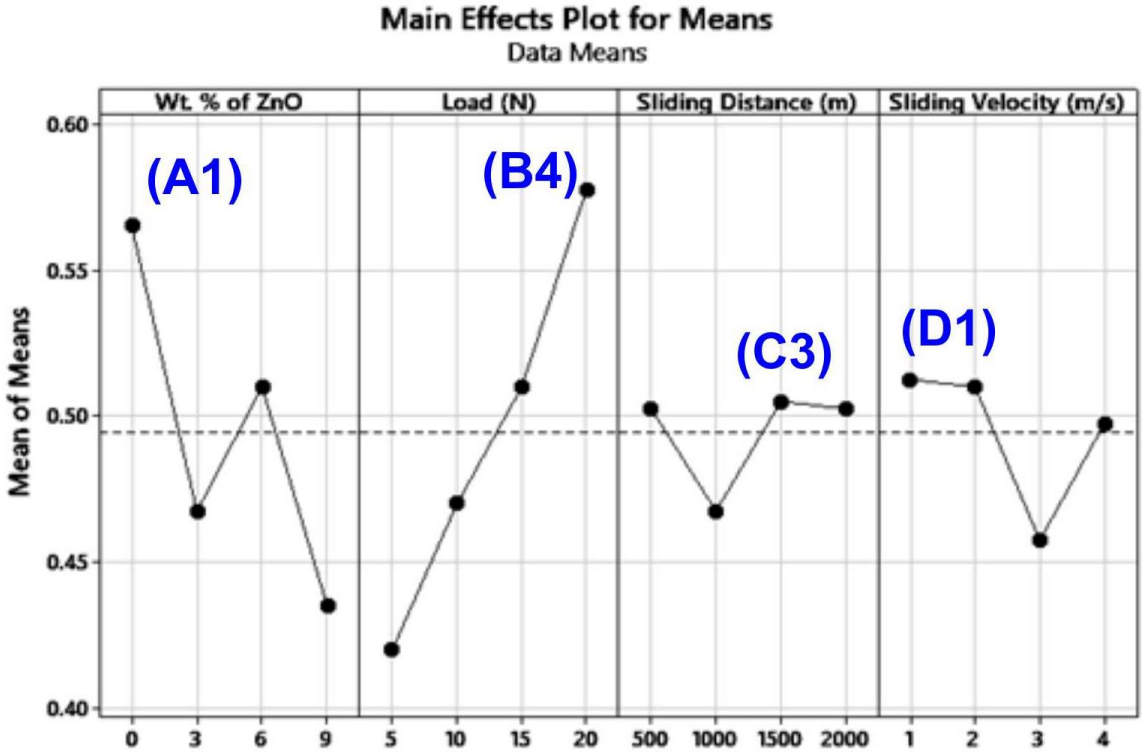

Fig. 14. Means plot of COF obtained from the Taguchi analysis for various input parameters wt.% of ZnO, L, D and V.

Moving forward, Tables 3-6 present the S/N ratios and Mean values for the WR and COF, respectively. Reinforced alloys experienced varying WRs, depending on the applied load. WR varied significantly in response to the applied load. According to Archard's law, which states that wear between surfaces is proportional to the normal pressure or load applied. This implies that when a load is applied, WR changes in proportion to the load. Therefore, the composite samples recorded a lower WR than alloy reinforced with Mg-3Al-ZnO, due to an increasing applied loads. With metal matrix reinforcements, wear coefficients decreased and volumetric losses reduced, since metal matrix particles were present. Mg-3Al particles reduced the rate of material removal, thereby increased the hardness of the composites at the same time. With low loads, WR was low, because the surface interacting pressure was lower as well as the existence of self-lubricating ZnO particles. WR was lower at low loads, because ZnO particles were self-lubricating and the surface interacting pressure was lower. Consequently, the rates of material removal from reinforced alloy were higher, because the surface debris adhered to the particles. It later resulted to a greater material removal, due to the high pressures developed at the interface of the alloys [21,25,26].

Table 3
Response table for S/N ratios for WR.

Level	Wt.% of ZnO	P (N)	D (m)	V (m/s)
I	-17.64	-14.18	-15.39	-15.57
II	-16.66	-15.14	-15.15	-15.85
III	-17.69	-16.06	-16.38	-15.49
IV	-11.34	-17.95	-16.42	-16.42
Delta	6.35	3.77	1.27	0.94
Rank	1	2	3	4

Table 4
Response table for Means for WR.

Level	Wt.% of ZnO	P (N)	D (m)	V (m/s)
I	7.917	5.314	6.034	6.284
II	6.961	5.892	5.976	6.673
III	7.694	6.619	6.963	6.147
IV	3.705	8.453	7.304	7.173
Delta	4.212	3.138	1.328	1.027
Rank	1	2	3	4

Table 5
Response table for S/N ratios for COF.

Level	Wt.% of ZnO	P (N)	V (m/s)	D (m)
I	4.981	7.740	5.998	5.885
II	6.879	6.591	6.866	5.958
III	5.897	5.870	6.051	7.016
IV	7.261	4.816	6.102	6.158
Delta	2.280	2.924	0.868	1.131
Rank	2	1	4	3

Table 6
Response table for Means for COF.

Level	Wt.% of ZnO	P (N)	V (m/s)	D (m)
I	0.5650	0.4200	0.5025	0.5125
II	0.4675	0.4700	0.4675	0.5100
III	0.5100	0.5100	0.5050	0.4575
IV	0.4350	0.5775	0.5025	0.4975
Delta	0.1300	0.1575	0.0375	0.0550
Rank	2	1	4	3

3.2.2 Contour plot analysis

Figs 15(a)-(f) show the contour plots for WR. The plots of WR *versus* P and wt.% of ZnO are shown in Fig. 15(a). It can be observed from the green plot that the reduction in WR was related to the increase in ZnO wt.% in the right corner. With regards to the P and D, plots 15(a)-(f) follow the same pattern. From Fig. 15(a), the dotted red line indicated the interaction between reinforcement and ZnO wt.% and D, and how it increased the WR. The plot also demonstrated how two parameters interacted for WR. Similarly, Figs 16(a)-(f) depict the contour plots for COF, including the plots for P *versus* wt.% of ZnO, P *versus* D and wt.% of ZnO *versus* D. The COF of the composite samples increased with the applied load, when it was subjected to the accelerate wear tests. According to the aforementioned factors, the proposed materials possessed higher wear resistance, due to their hardness and increased ZnO content. The WR increased with the slide velocity. A high sliding velocity V(m/s) resulted to a deformation. This can be attributed to the rapid removal of material, in addition to the matrix softening. Pins also lose material as a result of formation of layer on their surface layers, which peeled off as time passed. Reinforced alloy possessed a higher WR than the composites. Composites have a lower WR, because they contained large Mg-3Al-ZnO particles that served as hardeners and self-lubricants. Increased hardness improved both wear and seizure resistance properties of compounds, as similarly reported [23,24].

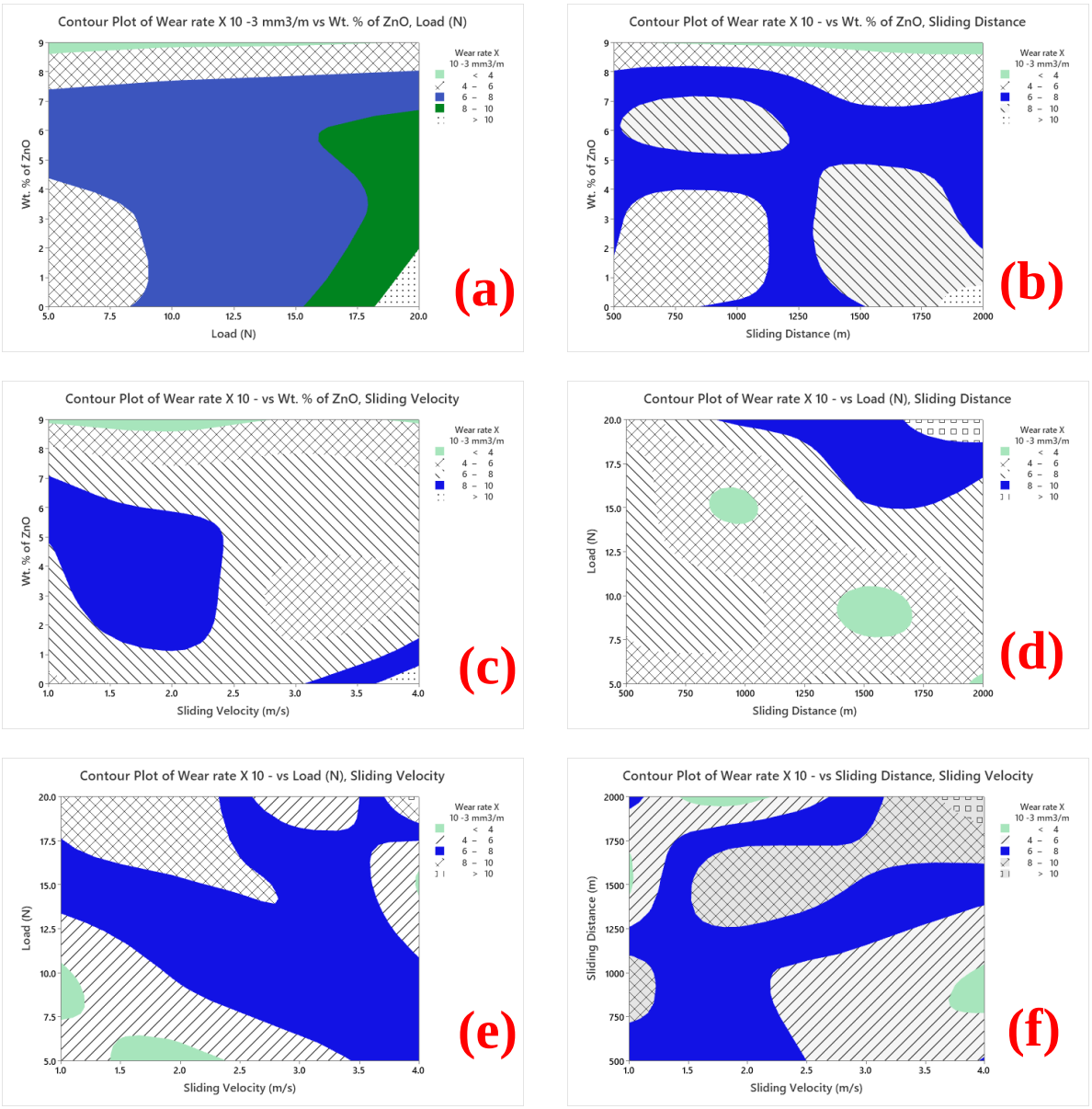

Fig. 15. Contour plots for WR obtained from the Taguchi analysis for various input parameters.

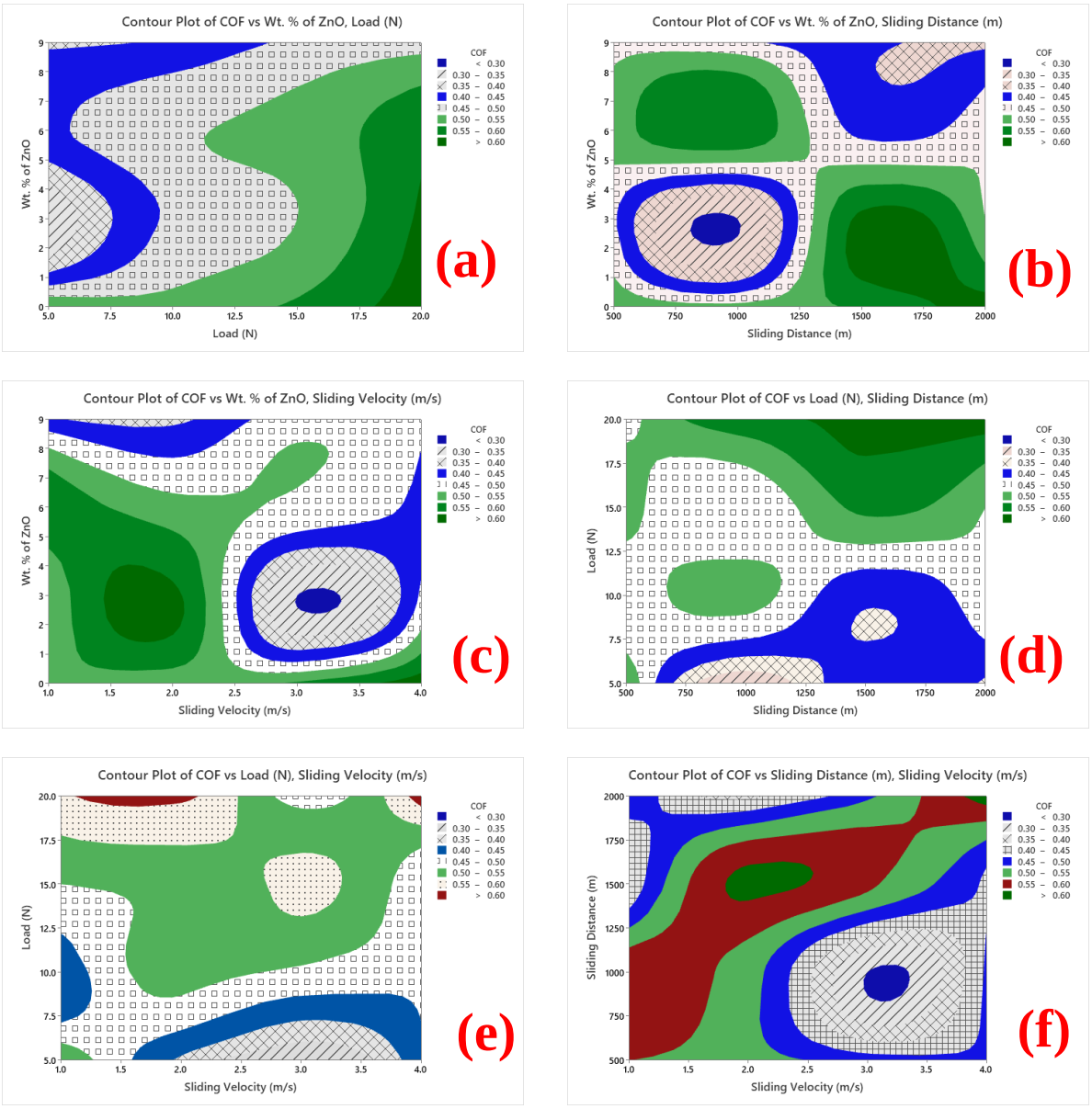

Fig. 16. Contour plots for COF obtained from the Taguchi analysis for various input parameters.

3.2.3 Interaction plot analysis

Figs 17 and 18 show the interaction plots for WR and COF, respectively. The improved wear resistance of Mg-3Al-ZnO can be traced to its ability to smooth and blunt the protrusions of the reinforcements during sliding. A layer of self-lubricating particles was formed when the sliding distance was increased, reducing wear. WR increased as the sliding distance increased for alloys with reinforced plates. The eventually pin failed, because it became weak when the contact surface was too hot, resulting to more material loss. Composites were more efficient at longer distances than reinforced alloys, due to their lower

hardness. The ZnO layer also exhibited benefit of reducing the WR of the composite matrix by serving as an insulating layer between the in-contact surfaces [21,24,25,26].

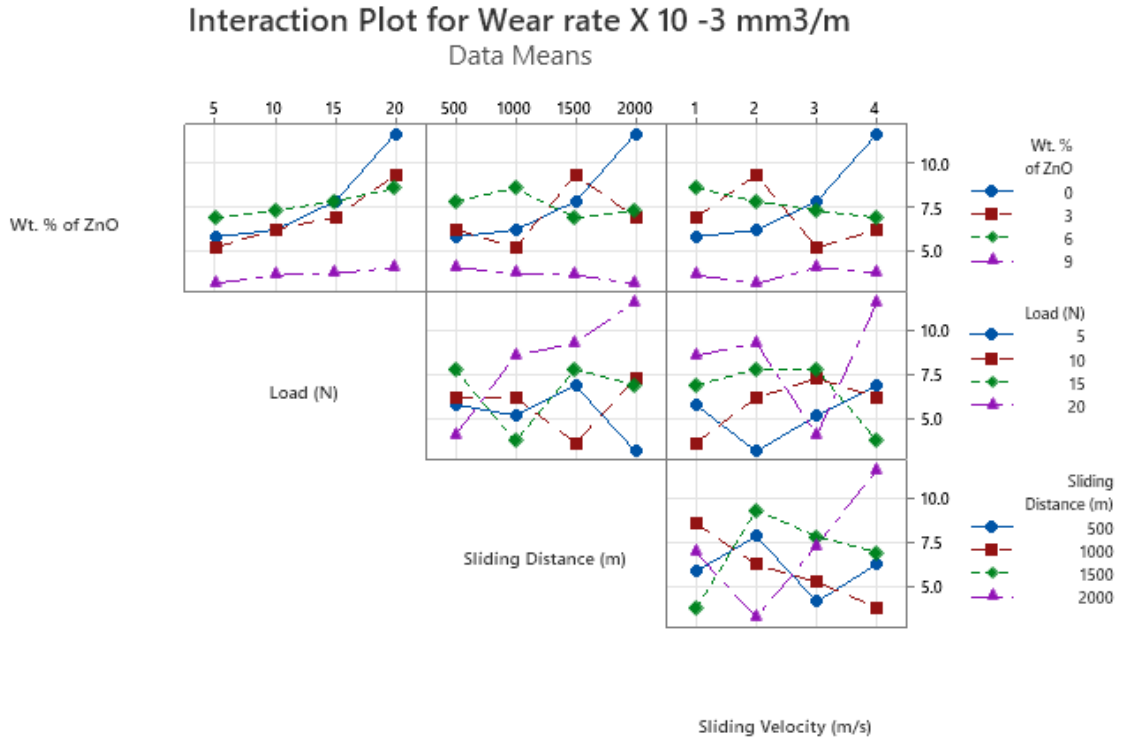

Fig. 17. Interaction plots of WR obtained for the input parameters wt.% of ZnO, L, D and V.

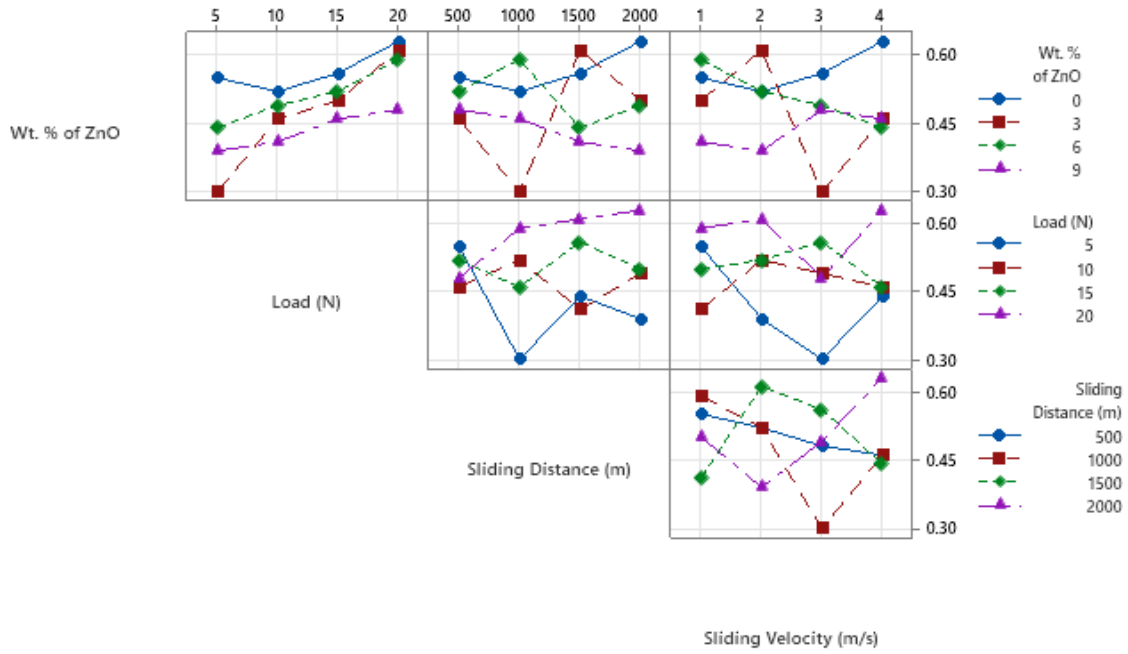

Fig. 18. Interaction plots of COF obtained for the input parameters wt.% of ZnO, L, D and V.

3.2.4 ANOVA

Using ANOVA, the distribution of WR and COF parameters, such as wt.% of ZnO, P, V and D were studied for Mg-3Al-ZnO composites. Table 7 presents ANOVA for WR. According to the F-value, the reinforcement and sliding distance accounted for the majority of the factors, while the P factor determined others. ANOVA for COF is presented in Table 8. It was evident that V recorded the greatest impact, followed by ZnO content, D and P [17], as presented in Table 8. Eqs (3) and (4) later show the regression equation for WR and COF, respectively.

Table 7
ANOVA for WR.

Source	DF	Adj SS	Adj MS	F-value	P-value
Wt.% ZnO	3	45.744	15.2479	20.08	0.017
P (N)	3	22.332	7.4441	9.80	0.046
V (m/s)	3	5.337	1.7789	2.34	0.251
D (m)	3	2.543	0.8477	1.12	0.465
Error	3	2.278	0.7592		
Total	15	78.234			

Table 8
ANOVA for COF.

Source	DF	Adj SS	Adj MS	F-value	P-value
Wt.% ZnO	3	0.037919	0.012640	4.56	0.122
P(N)	3	0.053119	0.017706	6.39	0.081
V (m/s)	3	0.003869	0.001290	0.47	0.727
D (m)	3	0.007769	0.002590	0.93	0.522
Error	3	0.008319	0.002773		
Total	15	0.110994			

3.2.5 Regression analysis

The important factors were used to create equations that could estimate the WR and COF of the composite samples, using the regression analysis. Therefore, regression Eqs (4) and (5) were developed specifically to select parameters and determine the optimal output variables. Figs 19 and 20 show the probability plots of WR and COF. Both Figs evidently depict that all the errors were within the limit by analysing for 95% of confidence intervals.

Regression equation for WR

$$\text{WR X } 10^{-3}\left(\frac{\text{mm}^3}{\text{m}}\right) = 6.569 + 1.348A_1 + 0.391A_2 + 1.124A_3 - 2.864A_4 - 1.255\,B_1 - 0.678\,B_2 + 0.049B_3 + 1.883B_4 - 0.535\,C_1 - 0.594\,C_2 + 0.394C_3 + 0.735C_4 - 0.285\,D_1 + 0.104\,D_2 - 0.423D_3 + 0.604\,D_4 \quad (4)$$

Regression equation for COF

$$\text{COF} = 0.4944 + 0.0706A_1 - 0.0269A_2 + 0.0156\,A_3 - 0.0594A_4 - 0.0744B_1 - 0.0244\,B_2 + 0.0156B_3 + 0.0831B_4 + \quad (5)$$

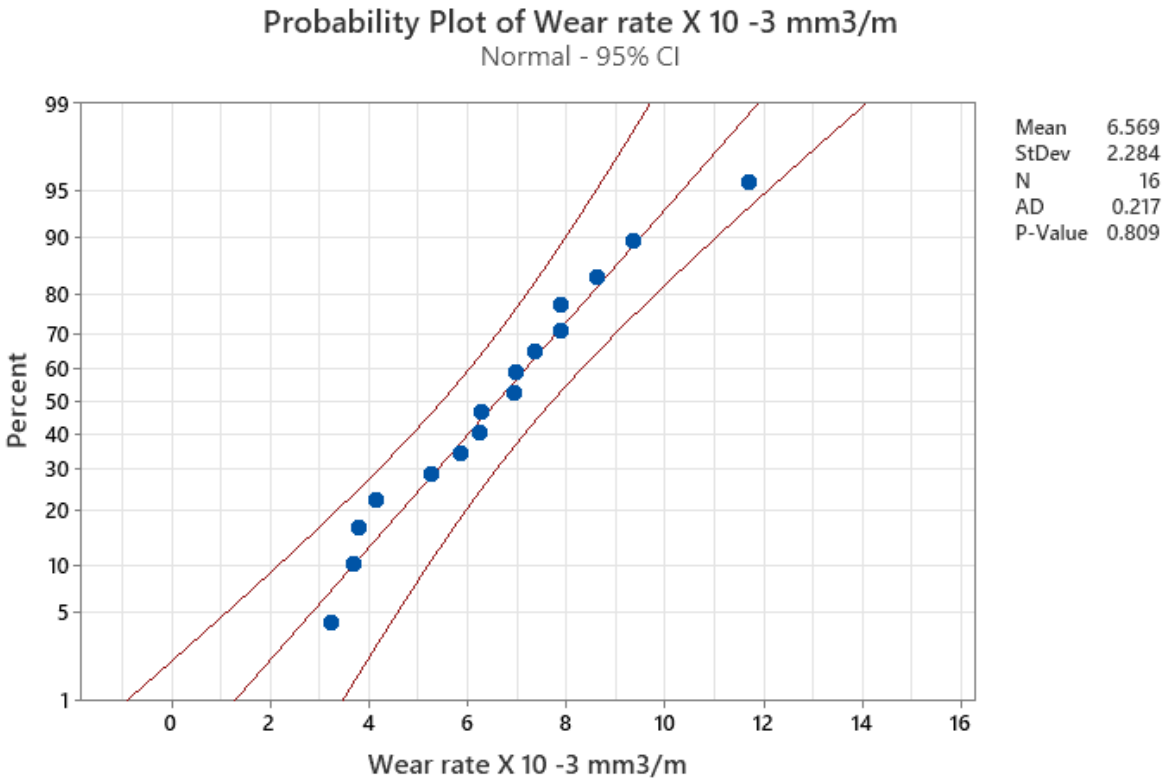

Fig. 19. Probability plot of WR.

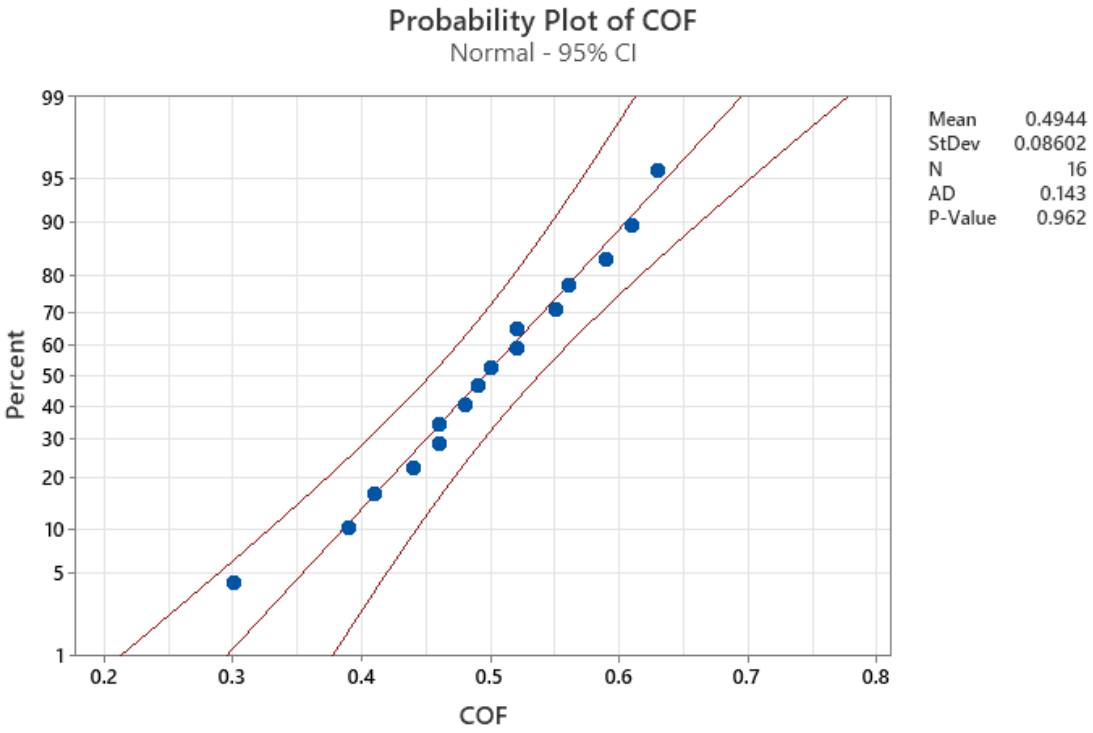

Fig. 20. Probability plot of COF.

3.2.6 Worn surface analysis

Considering the worn surface of Mg-3Al-ZnO composites shown in Figs 2(a)-(f), Figs 2(a) and (b) depict the worn surface of the composite with 3 wt.% of ZnO particle. It further shows the bluntly impaired regions, blister wear and huge flow of material with a lateral shift, caused by heavy plastic deformation. Figs 2(c) and (d) show the worn surface of the Mg-3wt.%Al-6wt.%ZnO composites. They also show the formation of small cavities and cracks on the surface of the wear track, which suggested dry sliding wear. On this surface, it can be further observed that rigid and hollow formed much more shallowly in the composites than they did in unreinforced alloys. This was resulted to the presence of reinforcing particles in the matrix materials. However, there was wear debris that accumulated on the wear track. This indicated that the wear occurred due to the presence of ZnO particles in the composites. The deformed plastic shrinkage was reduced significantly, because of the presence of ZnO particles. The ZnO particles acted as a barrier to displacements and thereby increased the wear resistance. When ZnO increased, both WR and COF decreased.

Additionally, Figs 2(e) and (f) show the worn surface images of the Mg-3wt.%Al-9wt.%ZnO composites. From the images, it was significantly observed that the ZnO particles

contribution was high, because the sample contained 9 wt. of ZnO particles. The wear track was also observed significantly from the SEM images. The distribution of the ZnO particles was uniform on the worn samples. It was observed that the composite samples experienced abrasive wear. This can be attributed to more wt.% of the ZnO particles presence in the matrix. All these occurrences contributed to the improved wear resistance of the ZnO reinforced Mg-based composites. Figs 2(a-d) depict the adhesion type of wear for all the specimen prepared, using PM method. Unreinforced magnesium alloy showed the plough mechanism confirmed by severe ploughing of material, due to the absence of hard reinforcement. The worn marks were visible in all directions. The inclusion of ZnO in Mg matrix decreased the removal of matrix material, as observed in Figs 2(b-d). The same phenomenon of low wear rate was observed on C/ZrO_2 composites at higher sliding velocity, as reported by Jha et al. [50] and Zhu et al. [51].

.

4. Conclusions

ZnO reinforced with Mg-3wt.%Al composites were fabricated, using PM technique and their microstructures and properties were studied. From the results obtained, the following concluding remarks can be deduced:

- SEM analysis of Mg-3Al-ZnO composite powder showed that the ZnO particles distributed uniformly within the matrix. This can be attributed to the correct choice of a suitable milling process. Similarly, the SEM image of Mg-3Al-ZnO sintered composites established proper distribution of ZnO within the matrix formed by Mg-3wt.%Al.
- XRD analysis established the presence of Mg-3Al matrix and ZnO peak in ball milled and sintered composite samples, and confirmed that the composites had no intermetallic phases.
- The experimental density and porosity of the sintered Mg-3wt.%Al, Mg-3wt.%Al-3wt.%ZnO, Mg-3wt.%Al-6wt.%ZnO and Mg-3wt.%Al-9wt.%ZnO composites were examined. It was evident that addition of reinforcements increased the density of the composites.
- The addition of 3-9 wt.% of ZnO to the matrix of Mg-3Al increased the hardness of the composites. Comparatively, Mg-3wt.%Al-9wt.%ZnO composite samples recorded the highest compressive strength, among the Mg-3Al alloy samples. Therefore, both compressive strength and hardness increased with an increase in inclusion of ZnO in Mg matrix at the expense of its ductility; ductility reduced. Therefore, all its mechanical

properties were not improved. However, both compressive strength and hardness are important properties in engineering and biomedical applications, especially where they are specifically and inevitably required.

- Corrosion resistance and wear behaviors of the composite samples were good, due to ZnO addition when compared with unreinforced alloy samples. Evidently, the corrosion resistance increased with an increase in ZnO, as validated with the SEM image of corroded sample. Therefore, for biomedical implant, the corrosion resistance of the implant material is a significant factor to be considered before selection of implants. Magnesium matrix composite is also suitable for biomedical applications.
- Abrasive wear was recorded on the samples with a high weight percentage of ZnO in the matrix, as observed from the SEM worn surface analysis.
- From the ANOVA analysis, it was evident that ZnO content was a highly significant factor that influenced the wear rate, while load mostly influenced COF of the composite samples during wear testing. The same results were evident from the S/N ratio analysis.

Finally, Mg-3Al-9wt.%ZnO matrix composite is an ideal material for industrial applications. It is suitable for other numerous real-world utilizations, considering the current increasing use of structural materials with enhanced wear resistance. Mg-3Al-9wt.%ZnO is an exceptional discontinuous reinforcement with outstanding CS, hardness and low density. Importantly, Mg-3Al-9wt.%ZnO composite has a potential of overcoming the cost obstacle for unlimited application in automotive parts and medical devices.

References

[1] W. Yu, X. Li, M. Vallet, L. Tian, High temperature damping behavior and dynamic Young's modulus of magnesium matrix composite reinforced by Ti_2AlC MAX phase particles, Mech. Mater. 129 (2019) 246-253. https://doi.org/10.1016/j.mechmat.2018.12.001

[2] T. Thirugnanasambandham, J. Chandradass, P.B. Sethupathi, M.L.J. Martin, Experimental study of wear characteristics of Al_2O_3 reinforced magnesium based metal matrix composites, Mater. Today Proc. 4 (2019) 211-218. https://doi.org/10.1016/j.matpr.2019.04.140

[3] J. Hou, W. Du, C. Zhao, X. Du, Z. Wang, S. Li, K. Liu, Study on the behaviors of multi-walled carbon nanotubes modified by gemini sulfonate dispersant and their reinforced magnesium matrix, Mater. Chem. Phys. 229 (2019) 279-285. https://doi.org/10.1016/j.matchemphys.2019.03.028

[4] C. Xie, H. Li, X. Zhou, C. Sun, Corrosion behavior of cold sprayed pure zinc coating on magnesium, Surf. Coat. Technol. 374 (2019) 797-806. https://doi.org/10.1016/j.surfcoat.2019.06.068

[5] F. Witte, N. Hort, C. Vogt, S. Cohen, K.U. Kainer, R. Willumeit, F. Feyerabend, Degradable biomaterials based on magnesium corrosion, C. Opin Solid State Mater. Sci. 12 (2008) 63-72. https://doi.org/10.1016/j.cossms.2009.04.001

[6] H. Yong, R. Li, Effect of particulate reinforcement on wear behavior of magnesium matrix composites, Trans. Nonferrous Met. Soc. China. 22 (2012) 2659-2664. https://doi.org/10.1016/S1003-6326(11)61514-8

[7] J. Capek, D. Vojtech, Effect of sintering conditions on the microstructural and mechanical characteristics of porous magnesium materials prepared by powder metallurgy, Mater. Sci. Eng. C. 43 (2014) 494-501. http://dx.doi.org/10.1016/j.msec.2013.10.014.

[8] M.E. Turan, Y. Sun, F. Aydin, H. Zengin, Y. Turen, H. Ahlatci, Effects of carbonaceous reinforcements on microstructure and corrosion properties of magnesium matrix composites, Mater. Chem. Phys. 218 (2018) 182-188. https://doi.org/10.1016/j.matchemphys.2018.07.050

[9] V.K. Bommala, M.G. Krishna, C.T. Rao, Magnesium matrix composites for biomedical applications: A review, J. Magnes. Alloy. 7 (2019) 72-29. https://doi.org/10.1016/j.jma.2018.11.001.

[10] K.B. Nie, K. Wu, X.J. Wang, K.K. Deng, Y.W. Wu, M.Y. Zheng, Multidirectional forging of magnesium matrix composites: Effect on microstructures and tensile properties, Mater. Sci. Eng. A. 527 (2010) 7364-7368. https://doi.org/10.1016/j.msea.2010.08.007

[11] A. Vahid, P. Hodgson, Y. Li, Reinforced magnesium composites by metallic particles for biomedical Applications, Mater. Sci. Eng. A. 685 (2017) 349-357. http://dx.doi.org/10.1016/j.msea.2017.01.017

[12] Y.L. Xi, D.L. Chai, W.X. Zhang, J.E. Zhou, Titanium alloy reinforced magnesium matrix composite with improved mechanical properties, Scr. Mater. 54 (2006) 19-23. https://doi.org/10.1016/j.scriptamat.2005.09.020

[13] P. Bansal, G. Singh, H.S. Sidhu, Investigation of surface properties and corrosion behavior of plasma sprayed HA/ZnO coatings prepared on AZ31 Mg alloy, Surf. Coat. Technol. 401 (2020) 126241. https://doi.org/10.1016/j.surfcoat.2020.126241

[14] R. Guan, A.F. Cipriano, Z. Zhao, J. Lock, D. Tie, T. Zhao, T. Cui, H. Liu, Development and evaluation of a magnesium–zinc–strontium alloy for biomedical applications — Alloy processing, microstructure, mechanical properties, and biodegradation, Mater. Sci. Eng. C. 33 (2013) 3661-3669. http://dx.doi.org/10.1016/j.msec.2013.04.054

[15] B. Selvam, P. Marimuthu, R. Narayanasamy, V. Anandakrishnan, K.S. Tun, M. Gupta, M. Kamaraj, Dry sliding wear behaviour of zinc oxide reinforced magnesium matrix nano-composites, Mater. Des. 58 (2014) 475-481. http://dx.doi.org/10.1016/j.matdes.2014.02.006

[16] R. Kumar, R. Singh, M. Singh, P. Kumar, On ZnO nano particle reinforced PVDF composite materials for 3D printing of biomedical sensors, J. Manuf. Process. 60 (2020) 268-282. https://doi.org/10.1016/j.jmapro.2020.10.027

[17] F. Chen, B. Tang, P. Jin, L. Zhang, W. Fei, Tensile properties and hot extrusion behavior of ZnO-coated Mg2B2O5w/6061 Al composites, Trans. Nonferrous Met. Soc. China. 25 (2015) 412-419. https://doi.org/10.1016/S1003-6326(15)63618-4

[18] M. Carboneras, L.S. Hernandez, J.A. Del Valle, M.C. García-Alonso, M.L. Escudero, Corrosion protection of different environmentally friendly coatings on powder metallurgy magnesium, J. Alloy. Compd. 496 (1–2) (2010) 442–448 https://doi.org/10.1016/j.jallcom.2010.02.043

[19] S.B. Bhosale, S. Bhowmik, A. Ray, Multi Criteria Decision Making For Selection Of Material Composition For Powder Metallurgy Process, Mater. Today Proc. 5 (2018) 4615-4620. https://doi.org/10.1016/j.matpr.2017.12.032

[20] S. Raynova, F. Yang, L. Bolzoni, Mechanical behaviour of induction sintered blended elemental powder metallurgy Ti alloys, Mater. Sci. Eng. A. 799 (2021) 140157. https://doi.org/10.1016/j.msea.2020.140157

[21] S.V. Alagarsamy, M. Ravichandran, Investigations on tribological behaviour of AA7075-TiO2 composites under dry sliding conditions, Ind. Lubr. Tribol. 71(9) (2019) 1064-1071. https://doi.org/10.1108/ILT-01-2019-0003

[22] S. Dharmalingam, R. Subramanian, M. Kok, Optimization of abrasive wear performance in aluminium hybrid metal matrix composites using taguchi-grey relational analysis, Proc. Inst. Mech. Eng. J: J. Eng. Tribol. 227 (7) (2013) 749-760. https://doi.org/10.1177/135065011246794

[23] B. Ashok Kumar, N. Murugan, Metallurgical and mechanical characterization of stir cast AA6061-T6–AlNp composite, Mater. Des. 40 (2012) 52-58. https://doi.org/10.1016/j.matdes.2012.03.038

[24] N. Radhika, R. Raghu, Dry Sliding Wear Behaviour of Aluminium Al–Si12Cu/TiB2 Metal Matrix Composite Using Response Surface Methodology, Tribol. Lett. 59 (2) (2015) 1-9. https://doi.org/10.1007/s11249-015-0516-3

[25] N. Radhika, R. Raghu, Evaluation of dry sliding wear characteristics of LM 13 Al/B4C composites, Tribol. Ind. 37 (1) (2015) 20-28

[26] N. Radhika, R. Raghu, Prediction of mechanical properties and modeling on sliding wear behavior of LM25/TiC composite using response surface methodology, Part. Sci. Technol. 36 (1) (2018) 104-111. https://doi.org/10.1080/02726351.2016.1223773

[27] A. Kumar, S. Kumar, N.K. Mukhopadhyay, Introduction to magnesium alloy processing technology and development of low-cost stir casting process for magnesium alloy and its composites, J. Magnes. Alloy. 6 (3) (2018) 245-254. https://doi.org/10.1016/j.jma.2018.05.006

[28] M.A. El Baradie, Manufacturing aspects of metal matrix composites J. Mater. Process. Technol. 24 (1) (1990) 261-272. https://doi.org/10.1016/0924-0136(90)90187-Y

[29] H. Zhou, L. Hu, Y. Sun, H. Zhang, C. Duan, H. Yu, Synthesis of nanocrystalline AZ31 magnesium alloy with titanium addition by mechanical milling, Mater. Charact. 113 (2016) 108-116. https://doi.org/10.1016/j.matchar.2016.01.014

[30] G. Mahajan, N. Karve, U. Patil, P. Kuppan, K. Venkatesan, Analysis of Microstructure, Hardness and Wear of Al-SiC-TiB_2 Hybrid Metal Matrix Composite, Indian J. Sci. Technol. 8 (2015) 101-105. https://doi.org/10.17485/ijst/2015/v8iS2/59081

[31] G.E.J. Poinern, S. Brundavanam, D. Fawcett, Biomedical Magnesium Alloys: A Review of Material Properties, Surface Modifications and Potential as a Biodegradable Orthopaedic Implant, Am. J. Biomed. Eng. 6 (2012) 218-240. https://doi.org/10.5923/j.ajbe.20120206.02

[35] A. Abbas, S. Huang, ECAP effects on microstructure and mechanical behavior of annealed WS2/AZ91 metal matrix composite, J. Alloy. Compd. 835 (2020), 155466, https://doi.org/10.1016/j.jallcom.2020.155466

[33] X.N. Gu, S.S. Li, X.M. Li, Y.B. Fan, Magnesium based degradable biomaterials: A review, Front. Mater. Sci. 8 (2014) 200-218. https://doi.org/10.1007/s11706-014-0253-9

[34] R. Kumar, Dr. C.N Chandrappa, Synthesis and Characterization of Al-SiC Functionally Graded Material Composites Using Powder Metallurgy Techniques, Int. J. Innov. Res. Technol. Sci. Eng. 3 (2014) 15464- 15471. https://doi.org/10.15680/IJIRSET.2014.0308054

[35] N. Saha, K. Keskinbora, E. Suvaci, Sintering, microstructure, mechanical, and antimicrobial properties of HAp-ZnO biocomposites, J. Biomed. Mater. Res. Part B: Appl. Biomater. 95 (2010) 430-440. https://doi.org/10.1002/jbm.b.31734

[36] A.K. Chaubey, S. Scudino, M. Samadi Khoshkhoo, K.G. Prashanth, N.K. Mukhopadhyay, B.K. Mishra, J. Eckert, High-strength ultrafine grain Mg-7.4%Al alloy synthesized by consolidation of mechanically alloyed powders, J. Alloy. Compd, 610 (2014) 456-461. https://doi.org/10.1016/j.jallcom.2014.05.029

[37] A.K. Chaubey, S. Scudino, M. Samadi Khoshkhoo, K.G. Prashanth, N.K. Mukhopadhyay, B.K. Mishra, J. Eckert, Synthesis and characterization of nanocrystalline Mg-7.4%Al powders produced by mechanical alloying, Metals, 3 (2013) 58-68. https://doi.org/10.3390/met3010058

[38] Y. Shadangi, K. Chattopadhyay, N. K. Mukhopadhyay, Powder metallurgical processing of Al matrix composite reinforced with AlSiCrMnFeNiCu high-entropy alloys: Microstructure, thermal stability, and microhardness, J. Mater. Res, 38 (2023) 248–264. https://doi.org/10.1557/s43578-022-00866-x

[39] Nandini Singh, Y. Shadangi, N. K. Mukhopadhyay, Phase evolution and thermal stability of low-density MgAlSiCrFe high-entropy alloy processed through mechanical alloying, Trans. Indian Inst, 73 (2020) 2377–2386. https://doi.org/10.1007/s12666-020-02039-y

[40] Y. Shadangi, S. Sharma, V. Shivam, J. Basu, K. Chattopadhyay, B. Majumdar, N.K. Mukhopadhyay, Fabrication of Al–Cu–Fe quasicrystal reinforced 6082 aluminium matrix nanocomposites through mechanical milling and spark plasma sintering, J. Alloy. Compd, 828, (2020) 154258. https://doi.org/10.1016/j.jallcom.2020.154258

[41] A. Suguna, S. Prabhu, M. Selvaraj, M. Geerthana, A. Silambarasan, M. Navaneethan, R. Ramesh, C. Sridevi, Annealing effect on photocatalytic activity of ZnO nanostructures for organic dye degradation, J. Mater. Sci. Mater. Electron, 33 (2022) 8868–8879. https://doi.org/10.1007/s10854-021-06942-y

[42] S. Prabhu, M. Pudukudy, S. Sohila, S. Harish, M. Navaneethan, D. Navaneethan, R. Ramesh, Y. Hayakawa, Synthesis, structural and optical properties of ZnO spindle/reduced graphene oxide composites with enhanced photocatalytic activity under visible light irradiation, Opt. Mater. 79 (2018) 186-195. https://doi.org/10.1016/j.optmat.2018.02.061

[43] S. Prabhu, S. Megala, S. Harish, M. Navaneethan, P. Maadeswaran, S. Sohila, R. Ramesh, Enhanced photocatalytic activities of ZnO dumbbell/reduced graphene oxide nanocomposites for degradation of organic pollutants via efficient charge separation pathway, Appl. Surf. Sci, 487 (2019) 1279-1288. https://doi.org/10.1016/j.apsusc.2019.05.086

[44] S. Prabhu, M. Pudukudy, S. Harish, M. Navaneethan, S. Sohila, K. Murugesan, R. Ramesh, Facile construction of djembe-like ZnO and its composite with g-C3N4 as a visible-light-driven heterojunction photocatalyst for the degradation of organic dyes, Mater. Sci. Semicond, 106 (2020) 104754. https://doi.org/10.1016/j.mssp.2019.104754

[45] C. Jayakrishnan, S.R. Sheeja, J. Duraimurugan, S. Prabhu, R. Ramesh, G. Suresh Kumar, K.G. Subhash, Mohd Shkir, M. R. Pallavolu, Synthesis of dumbbell-shaped ZnO nanostructures for energy storage and photocatalytic dye degradation applications, Mater Technol, 37 (14) (2022) 3006-3016. https://doi.org/10.1080/10667857.2022.2107821

[46] M. Satheesh, M. Pugazhvadivu, Investigation on physical and mechanical properties of Al6061-silicon carbide (SiC)/Coconut shell ash (CSA) hybrid composites. Phys B Condens Matter, 572 (2019) 70–75. https://doi.org/10.1016/j.physb.2019.07.058

[47] S. Jayasathyakawin, M. Ravichandran, Experimental Investigations on effect of silicon carbide on microstructure and mechanical properties in Mg-3 wt% Al alloy matrix using powder metallurgy, Silicon, 14 (2022) 9163-9173. https://doi.org/10.1007/s12633-022-01834-0

[48] L. Azaath, Mamundi, Experimental investigations on the mechanical properties, microstructure and corrosion effect of Cu-20Al-4Ni/SiC composites synthesized using powder metallurgy route. Silicon, 14 (11) (2022) 5993–6002. https://doi.org/10.1007/s12633-021-01363-2

[49] K. S. Tun, M. Gupta, Improving mechanical properties of magnesium using nano-yttria reinforcement and microwave assisted powder metallurgy method', Compos Sci Technol, 67 (13) (2007) 2657-2664. https://doi.org/10.1016/j.compscitech.2007.03.006.

[50] N. Jha, A. Badkul, D. P. Mondal, S. Das, M. Singh, Sliding wear behaviour of aluminum syntactic foam: a comparison with Al–10 wt.% SiC composites, Tribol Int 44 (2011) 220–231. https://doi.org/10.1016/j.triboint.2010.10.004

[51] H. G. Zhu, Y. L. Ai, J. Min, Q. Wu, H. Z. Wang, Dry sliding wear behavior of Al-based composites fabricated by exothermic dispersion reaction in an Al–ZrO2–C system, Wear 268 (2010) 1465–1471. https://doi.org/10.1016/j.wear.2010.02.023

[52] G. Veerappan, M. Ravichandran, M. Meignanamoorthy, V. Mohanavel, Characterization and properties of silicon carbide reinforced Ni-10Co-5Cr (Superalloy) matrix composite produced via powder metallurgy route. Silicon, 13 (4) (2021) 973–984. https://doi.org/10.1007/s12633-020-00455-9

[53] D. M. Jarząbek, The impact of weak interfacial bonding strength on mechanical properties of metal matrix – Ceramic reinforced composites. Compos. Struct, 201 (2018) 352–362. https://doi:10.1016/j.compstruct.2018.06.071

[54] M. Satheesh, M. Pugazhvadivu, Investigation on physical and mechanical properties of Al6061-silicon carbide (SiC)/coconut shell ash (CSA) hybrid composites, Physica B Condens. 572 (2019) 70-75. https://doi.org/10.1016/j.physb.2019.07.058